

Philipp EIBL, Bsc

Scale-Up Simulations of Cell Culture Bioreactors

MASTER'S THESIS

to achieve the university degree of
Diplom-Ingenieur

Master's degree programme: Chemical and Process Engineering

submitted to
GRAZ UNIVERSITY OF TECHNOLOGY

Supervisor:
Univ.-Prof. Dipl.-Ing. Dr. Johannes KHINAST
INSTITUTE FOR PROCESS AND PARTICLE ENGINEERING

Second Supervisor:
Ass.-Prof. Dipl.-Ing. Dr. Heidrun GRUBER-WÖLFER
INSTITUTE FOR PROCESS AND PARTICLE ENGINEERING

Graz, November 2017

EIDESSTATTLICHE ERKLÄRUNG

Ich erkläre an Eides statt, dass ich die vorliegende Arbeit selbstständig verfasst, andere als die angegebenen Quellen/Hilfsmittel nicht benutzt, und die den benutzten Quellen wörtlich und inhaltlich entnommenen Stellen als solche kenntlich gemacht habe. Das in TUGRAZonline hochgeladene Textdokument ist mit der vorliegenden Masterarbeit identisch.

Datum

Unterschrift

AFFIDAVIT

I declare that I have authored this thesis independently, that I have not used other than the declared sources/resources, and that I have explicitly indicated all material which has been quoted either literally or by content from the sources used. The text document uploaded to TUGRAZonline is identical to the present master's thesis.

Date

Signature

Acknowledgement

First of all I would like to thank Christian Witz, who was always ready to lend an ear and provided helpful guidance and support. Not only did he accompany me in this master's thesis, he introduced me into the sprawling field of computational fluid dynamics when I started my bachelor thesis two years ago.

I would also like to thank Prof. Johannes Khinast for the possibility of conducting this thesis and for the possibility to further work on this project at the Institute for Process and Particle Engineering.

Special thanks go to my family and friends for keeping me motivated and dedicated in the recent months.

Contents

1	Introduction	1
1.1	Lattice Boltzmann Method	1
1.2	Turbulence model	4
1.3	Gas phase model	5
1.4	Non-Newtonian fluids	8
1.5	Species transport model	9
1.6	Mass transfer model	11
1.7	Simulated reactors	12
1.8	Aim of this work	13
2	Scale-Up Strategies	14
2.1	Scale-Up parameters	14
2.1.1	Mixing Time	14
2.1.2	$k_L a$ -value	15
2.1.3	Hold-Up	16
2.1.4	Power Input	16
2.1.5	Shear rate	16
2.2	Dimensional analysis	17
2.3	Correlations	19
3	Internal Tank Geometries	25
3.1	Stirrer geometries	26
3.2	Heat exchanger	27
3.3	Sensors	29
4	Species Transport	31
4.1	Initialisation	31
4.2	Boundary handling	32
4.3	Gas-Phase coupling	33
4.4	Calculation of mass transfer	36
5	Simulation improvements	38
5.1	Lattice unit correction	38
5.2	Parcel approach stability	39
5.3	Serial simulation	41

6	Scale-Up Simulations	44
6.1	Mixing times	47
6.2	k_1a -value	51
6.3	Holdup	52
6.4	Shear Rate	53
6.5	Summary	55
7	Small scale Simulations	56
7.1	Mixing times	57
7.2	k_1a -value	58
7.3	Shear Rates	59
7.4	Non-Newtonian fluid	61
7.5	Summary	62
8	Summary	63
A	Appendix	69
A.1	Nomenclature	70
A.2	k_1a measurements on the 150 L reactor	72
A.3	Hold-Up measurements on the 150 L reactor	73

Abstract

A simulation code for gassed stirred tanks is used for the simulation of different reactor sizes with different operating conditions. A new stirrer type and new sensor geometries inside the tank are implemented, as well as a porous media model for small heat exchanger tubes. The boundary condition of the existing species transport model is changed to free-slip. The mixing behaviour for different gassing rates is improved with a new consideration of the gas phase coupling force. Mass transfer coefficients yield very good results for a newly refined mass transfer time step. For small stirrer speeds the blade tip velocity may not be the highest velocity inside the reactor, therefore the bubble rising velocity is considered in the initialisation of the simulation. With a newly implemented serial simulation routine the mixing times, mass transfer coefficients, holdup-values, shear rates and power numbers are in good agreement with literature correlations and measurements.

Kurzfassung

Ein bestehender Simulationscode für die Simulation von begasten Rührkesseln wird für verschiedene Reaktorgrößen verwendet. Neben der Implementierung von neuen Geometrien wie Rührer und Sensoren im Reaktor wird ein Modell für die Strömung durch poröse Medien implementiert um Wärmetauscherbündel mit kleinen Rohren zu simulieren. Die Randbedingung des konvektiven Stofftransportmodells wird auf "free-slip" geändert. Durch eine neu implementierte Rückkoppelung von der Gas-Phase auf die Flüssigphase, zeigt sich ein konsistentes Mischverhalten für unterschiedliche Begasungsraten. Der Zeitschritt für den Stofftransport von Gas in die Flüssigphase wird verkürzt, wodurch sich $k_L a$ -Werte ergeben die gut mit Messungen übereinstimmen. Die höchste Geschwindigkeit im Reaktor kann bei langsamen Rührerdrehzahlen durch die Gasblasen gegeben sein, dies wird nun für die Initialisierung der Simulation beachtet. Außerdem wird eine Routine für mehrere Simulationen in Serie implementiert. Die Ergebnisse zeigen gute Übereinstimmung der Mischzeiten, Stoffübergangskoeffizienten, Holdup-Werte, Scherraten und Leistungseintrag mit experimentellen Daten und Korrelationen aus veröffentlichter Literatur.

Chapter 1

Introduction

1.1 Lattice Boltzmann Method

The field of computational fluid dynamics has gained a lot of attention in recent years because nowadays computational resources allow for sophisticated simulations of engineering problems on a single workstation.

Most of the established software packages available solve the Navier-Stokes equations. In this thesis a different approach is used, the so-called Lattice Boltzmann Method (LBM). In the usual macroscopic continuum approach using the Navier-Stokes equations the variables like density, velocity and pressure are directly calculated on each calculation node. LBM is a mesoscopic method, which comes from the earlier microscopic models that allow for simulations on a molecular level, based on very simple collision and bounce-back rules. These rules are applied in LBM not only on single particles, but on particle populations with a probability density function $f(\mathbf{x}, \mathbf{c}, t)$ which is described by the Boltzmann equation.

The probability density function gives the probability for a flow in a specific direction at every lattice point in space and time. In the LBM, space is discretized in a uniform grid and on every grid node a set of velocity vectors is defined. Only certain choices of velocity vectors are allowed in order to assure the applicability of the Lattice Boltzmann Method. In this thesis the widely used D3Q19 model is applied, which is a 3D-model with 19 velocity vectors on each grid node [19].

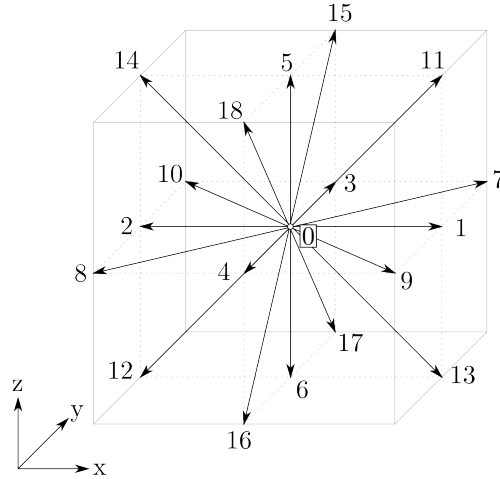


Figure 1.1: D3Q19-Lattice

In LBM the following discretized form of the Boltzmann equation is used [20, p. 23]:

$$f_i(\mathbf{x} + \mathbf{c}_i, t + 1) - f_i(\mathbf{x}, t) = \Omega_i(\mathbf{x}, t) \quad (1.1)$$

The right hand side with Ω_i denotes the collisional operator. The most commonly used correlation for this collisional operator is postulated by Bhatnagar, Gross and Krook [2]:

$$\Omega_i = -\frac{1}{\tau} f_i^{neq} \quad (1.2)$$

τ is the relaxation time of the fluid and is a crucial parameter in LBM. It defines the macroscopic viscosity of the fluid. f_i^{neq} is the difference of the present distribution function f_i to an equilibrium distribution function f_i^{eq} . This equilibrium distribution function follows the well known Maxwell-Boltzmann distribution [20, p. 30].

$$f_i^{eq} = w_i \rho \left[1 + \frac{\mathbf{c}_i \cdot \mathbf{u}}{c_s^2} + \frac{(\mathbf{c}_i \cdot \mathbf{u})^2}{2c_s^4} - \frac{\mathbf{u} \cdot \mathbf{u}}{2c_s^2} \right] \quad (1.3)$$

Here c_s is the speed of sound, \mathbf{c}_i denotes the components of each lattice vector, \mathbf{u} is the macroscopic fluid velocity, ρ is the fluid density and w_i a weighting factor for each lattice vector that is given for the D3Q19 grid.

If all the f_i values are known, the macroscopic variables can be calculated [20, p. 25]:

$$\rho = \sum_i f_i \quad (1.4)$$

$$\mathbf{u} = \frac{1}{\rho} \sum_i f_i \mathbf{c}_i \quad (1.5)$$

In equation 1.1 it can be seen that the difference in time for each calculation is equal to 1. This timestep is achieved by converting the physical quantities into dimensionless lattice units, in which also the length between two grid nodes is set to be 1. Thus, a conversion factor is assigned to each basis unit. The conversion factor for length is then simply a reference length (in this thesis the reactor diameter) divided by the number of grid nodes that shall be used in the simulation.

The conversion factor for time is defined by setting a fixed value for the tip speed in lattice units. LBM is valid in the limit of low Mach numbers [20, p. 29], therefore the ratio between the highest velocity in our simulation (e.g. tip speed velocity) and the speed of sound (c_s is always $1/\sqrt{3}$ for a D3Q19 grid) shall be significantly lower than 1. The tip speed is therefore fixed to 0.01 lattice units. The conversion factor for time can then be obtained:

$$\delta t = \frac{u_{blade,l}}{u_{blade,p}} \delta x \quad (1.6)$$

where l denotes lattice units, p stands for physical units and Δx is the conversion factor for length. Furthermore, the conversion factor for mass is obtained by setting the fluid density to 8.0 in lattice units:

$$\delta m = \frac{\rho_{liquid,p}}{\rho_{liquid,l}} (\delta x)^3 \quad (1.7)$$

In the following step these conversion factors are now used to convert the fluid viscosity to lattice units to obtain the relaxation time τ :

$$\tau = \frac{\nu}{c_s^2} + \frac{1}{2} \quad (1.8)$$

1.2 Turbulence model

The turbulent length scale in a stirred tank reactor usually is smaller than the grid size by orders of magnitude. A direct numerical simulation up to this length scale would require vastly more computational effort. In order to predict the turbulent behaviour on the sub-grid-scale a Smagorinsky Large-Eddy-Simulation is implemented, which is described by [18, p. 17]. This model can be used for Newtonian as well as non-Newtonian liquids.

The idea behind the Large-Eddy-Simulation is to model the energy cascade on the sub-grid-scale by assuming an isotropic turbulence, which is valid in the small scale. This additional energy is considered as an additional turbulent viscosity of the fluid:

$$\nu_t = (C\Delta)^2 S \quad (1.9)$$

S equates to the resolved magnitude of the shear rate, Δ is the cell length (e.g. 1) and C is the Smagorinsky constant, which is shown to be 0.1 in stirred tank reactors [6].

$$(C\Delta)^2 S = \frac{1}{6} \left(\sqrt{\nu^2 + 18C^2 \sqrt{\Pi_{\alpha\beta} \Pi_{\alpha\beta}}} - \nu \right) \quad (1.10)$$

$\Pi_{\alpha\beta}$ stands for the so called non-equilibrium stress tensor and is given by [18, p. 17]:

$$\Pi_{\alpha\beta} = \sum_{i=1}^{19} \mathbf{c}_{i\alpha} \mathbf{c}_{i\beta} (f_i - f_i^{eq}) \quad (1.11)$$

Finally, the turbulent viscosity is simply added onto the fluid viscosity to yield the effective viscosity.

$$\nu_{eff} = \nu_{app} + \nu_t \quad (1.12)$$

1.3 Gas phase model

The bubble motion is described by Lagrangian particle tracking, therefore every bubble has a distinct radius and position. The bubbles are initialised at the gas sparger at the bottom and interact with the fluid phase through a coupling force.

The bubble movement is calculated by solving Newtons equation of motion, as it is described by [16, p. 90]. The fluid properties are sampled onto the bubble location with a polynomial function[16, p. 81]:

$$\zeta(\mathbf{x} - \mathbf{x}_p) = \frac{15}{16} \left[\frac{(\mathbf{x} - \mathbf{x}_p)^4}{n^5} - 2 \frac{(\mathbf{x} - \mathbf{x}_p)^2}{n^3} + \frac{1}{n} \right], |\mathbf{x} - \mathbf{x}_p| \leq n \quad (1.13)$$

The probability of collision of a bubble with a fictitious second bubble at the current time step is calculated according to [16, p. 52]:

$$P_{coll} = \frac{\pi}{4} (d_{p,i} + d_{p,j})^2 |\mathbf{u}_{p,i} - \mathbf{u}_{p,j}| n_p \Delta t, \quad (1.14)$$

where $d_{p,i}$ and $d_{p,j}$, $\mathbf{u}_{p,i}$ and $\mathbf{u}_{p,j}$ are the bubble diameter and velocity of the bubble and the collision partner. The properties of the collision partner are based on the local statistics around the real bubble. n_p is the number of bubbles per volume and Δt the contact time. A random number between 0 and 1 is compared to the collision probability, if this number is smaller than P_{coll} than the bubbles collide. Coalescence occurs if the contact time between the collision partners is larger than the film rupture time.

A bubble can also break up into smaller bubbles by interaction with the turbulent eddys. If a turbulent eddy is in the length scale of the bubble it can break the bubble. Smaller eddies do not have enough energy to break a bubble whereas larger eddies result in bubble transport.

Parcel approach

High gassing rates in large reactors can result in a very large number of lagrangian particles. For each of these particles the bubble calculation has to be performed resulting in high demands on memory and computation time. Therefore a parcel approach is applied in the simulations[16, p. 50]. A parcel acts as a representative particle that stands for several bubbles that are located in the region of the parcel.

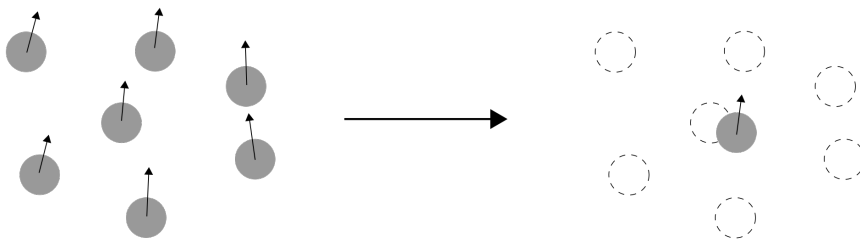


Figure 1.2: Parcel approach for the gas phase

In figure 1.2 the parcel approach is visualised. Rather than calculating the exact position and velocity of each bubble, only the parcel shown on the right is tracked with the lagrangian approach. The number of particles as well as the diameter of the bubbles is stored for each parcel, therefore the influence of these bubbles is considered in the gas phase coupling and the mass transfer model.

If bubble breakup or coalescence occurs only the number of particles in a parcel and the diameter is changed. No additional lagrangian particles or parcels are added in case of a breakup.

Backward coupling force

The influence of the lagrangian particles onto the eulerian flow field is described by a coupling force which is included in the fluid simulation. It is described by [16, p. 51] with the following relation:

$$\mathbf{F}_{p,i \rightarrow l,j} = -\frac{\zeta_j n_p}{V_{cell,j}} (\mathbf{F}_D + \mathbf{F}_L + \mathbf{F}_A) \quad (1.15)$$

In this equation ζ_j is the mapping function which is described above, n_p is the number of particles in a parcel, V_{cell} is the eulerian cell volume and \mathbf{F}_D , \mathbf{F}_L , \mathbf{F}_A are the drag force, lift force and added mass force [16, p. 91].

1.4 Non-Newtonian fluids

In general the shear rate and shear stress is given by following relations [13, p. 8]:

$$\dot{\gamma} = \frac{du}{dy} \quad (1.16)$$

$$\tau = \mu \dot{\gamma} \quad (1.17)$$

In the simulation code not only Newtonian fluids with constant viscosity μ can be simulated but also power-law fluids, which are also called generalized Newtonian fluids. In this model the apparent viscosity μ_{app} depends on the shear rate and on the consistency index and power law index of the fluid:

$$\mu_{app} = K S^{n-1} \quad (1.18)$$

The shear rate is given as the magnitude of the shear rate tensor and can be obtained within the LBM framework with the following relation [4]:

$$S = \sqrt{2S_{\alpha\beta}S_{\alpha\beta}} = \sqrt{\frac{\epsilon}{\nu_{app}}} \quad (1.19)$$

ν_{app} is the apparent viscosity which is the adjusted liquid viscosity after application of the turbulence model.

The energy dissipation can be calculated with the following equation [22]:

$$\epsilon = \frac{9\nu}{2\rho^2\tau^2} \sum (\Pi_{\alpha\beta}\Pi_{\alpha\beta}) \quad (1.20)$$

where $\Pi_{\alpha\beta}$ denotes the non-equilibrium stress tensor that is obtained from the distribution functions on each lattice node:

$$\Pi_{\alpha\beta} = \sum_{i=1}^{19} \mathbf{c}_{i\alpha} \mathbf{c}_{i\beta} (f_i - f_i^{eq}) \quad (1.21)$$

1.5 Species transport model

In general if a soluble substance is introduced into the liquid system two transport phenomena occur: convection and diffusion. Therefore the following general differential equation describes the transport process:

$$\frac{\partial c}{\partial t} = \nabla \cdot (D \nabla c) - \nabla \cdot (\mathbf{u}c) \quad (1.22)$$

It is shown that this advection-diffusion equation can be calculated within the LBM framework in a similar manner to the fluid calculation but with a different equilibrium distribution function f_{σ}^{eq} [15]:

$$f_{\sigma,i}^{eq} = w_i * \rho_{\sigma} (1 + 3\mathbf{c}_i \cdot \mathbf{u}) \quad (1.23)$$

The relaxation time for this model can be obtained from the diffusion coefficient:

$$D_{\sigma} = \frac{1}{3} \left(\tau_{\sigma} - \frac{1}{2} \right) \quad (1.24)$$

For the calculation of the necessary relaxation time, the diffusion coefficient has to be converted into lattice units with the given conversion factors from the fluid phase LBM. For the simulations in this thesis the relaxation time τ_{σ} tends to be close to 0.5. In this region the LBM becomes very unstable. In order to achieve an acceptable relaxation time the timestep and spatial resolution of the simulation would have to be significantly finer. This is not applicable due to memory and computation time limitations.

The diffusion mainly accounts for the microscopical mixing process inside the stirred tank reactor. Large scale mixing processes mainly operate in the turbulent regime. The dimensionless Peclet number $Pe = Lu/D$ describes the ratio between convective and diffusive transport processes and can be expressed by the Reynolds and Schmidt number:

$$Pe = Re \cdot Sc = \frac{Lu}{D} \quad (1.25)$$

In the turbulent regime, the Reynolds $Re = ND^2/\nu$ number is very high. The Schmidt number $Sc = \nu/D$ is far greater than unity since the diffusion coefficient D is lower than the kinematic viscosity ν of the fluid. Therefore the Peclet number indicates a convection dominated transport process and a purely convective species transport model is applied.

In this model the current fluid velocity is projected onto a D3Q27-Lattice, which is a valid grid type for LBM simulations that also takes into account vectors pointing to the corners of each calculation cell [19]. As we already have seen in the standard LBM each vector represents a probability value of fluid flow in each direction and velocity. In this species transport model each vector represents a certain mass of substrate flowing into each direction. The velocities are solely given by the preceding standard fluid LBM and are not relaxed unphysically like in other LBM species transport models.

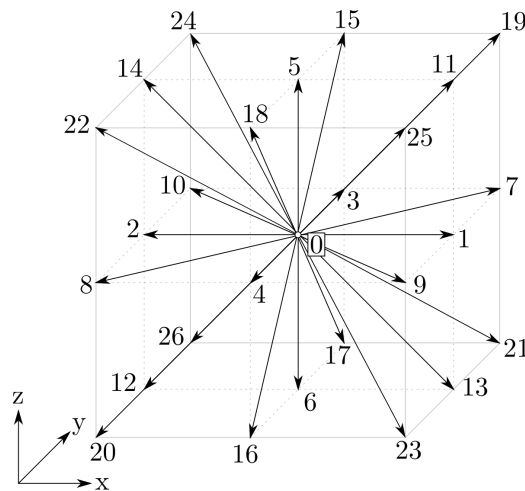


Figure 1.3: D3Q27-Model

Setting the species vectors from the information of the velocity field can be viewed as the collision step of this species model. Afterwards the streaming step is carried out in a similar manner to the standard LBM model.

It is obvious that without consumption of substrate the global mass of substrate must be constant, but mass can not be conserved locally as it passes through certain calculation cells. In the fluid region the current model gives a valid representation of the mixing effects, however on the boundary nodes certain instabilities can occur. This problem is handled in chapter 4 of this thesis, as well as the coupling of gas-phase forces with the species transport.

1.6 Mass transfer model

Since the bubble movement as well as the species transport inside the fluid is simulated, the resulting oxygen concentration in each cell can be obtained. For each bubble parcel the mass transfer is calculated and then added onto the concentration profile. At first the mass transfer coefficient based on the liquid phase k_l is evaluated with Higbie's penetration theory [8, p. 281]:

$$k_l = 2\sqrt{\frac{D}{\pi t_c}} \quad (1.26)$$

whereas D is the diffusion coefficient and t_c is the contact time between gas and liquid phase. The contact time is estimated to be the time it takes for the bubble to move through the fluid field for a length equivalent to the bubble diameter:

$$t_c = \frac{d_{bubble}}{u_{rel}} \quad (1.27)$$

where u_{rel} is the relative velocity between the fluid field and the gas bubble. The saturation concentration of oxygen can be calculated by the following equation:

$$c^* = \frac{p_{bubble} * y_{O_2}}{H_{x,p}} * \frac{\rho_{H_2O}}{MW_{H_2O}} \quad (1.28)$$

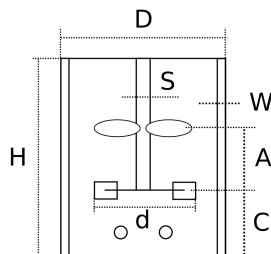
$H_{x,p}$ denotes the Henry constant [14]. With the surface area A of the bubbles, that can be obtained easily from the given particle size and number of bubbles in each parcel, the mass transfer can now be calculated:

$$\Delta m = k_l * A * (c^* - c) * MW_{O_2} * \Delta t \quad (1.29)$$

The timestep Δt is based on the LBM time step and the transferred mass Δm is then added to the oxygen concentration field at the given location.

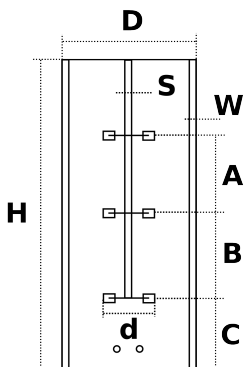
1.7 Simulated reactors

3 different vessel geometries were tested in this thesis. In each vessel a ring gas sparger is attached at the bottom. The geometry of each is given as follows.



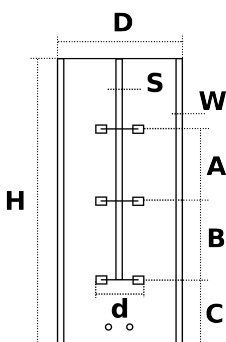
V	Volume	25 l
D	Vessel diameter	0.265 m
H	Height	0.453 m
d_1	Rushton diameter	0.127 m
d_2	Pitched blade diameter	0.135 m
α	Pitched angle	60°
C	Clearance	0.105 m
S	Shaft diameter	0.02 m

Figure 1.4: Geometry of the 25 liter vessel



V	Volume	150 l
D	Vessel diameter	0.440 m
H	Height	1.015 m
d	Impeller diameter	0.147 m
A	Impeller distance	0.295 m
B	Impeller distance	0.295 m
C	Clearance	0.170 m
S	Shaft diameter	0.050 m
W	Baffle width	0.045 m
n	Baffle number	4

Figure 1.5: Geometry of the 150 liter vessel



V	Volume	19.3 m ³
D	Vessel diameter	2.2 m
H	Height	5.075 m
d	Impeller diameter	0.735 m
A	Impeller distance	1.475 m
B	Impeller distance	1.475 m
C	Clearance	0.85 m
S	Shaft diameter	0.25 m
W	Baffle width	0.225 m
n	Baffle number	4

Figure 1.6: Geometry of the 19 m³ vessel

1.8 Aim of this work

This introduction gave an overview of the models that are used in the simulations and the reactor sizes that are simulated. For the small reactor an elephant ear impeller is specified which is implemented in this thesis. Other implementations are sensors inside the fluid region and a porous media model for the heat exchangers, which is described in chapter 3.2.

Starting from the 150 l reactor a Scale-Up by a geometric factor of 5 is performed. The resulting reactor with a volume of 19 m³ is then tested in different operating regimes, with different quantities kept constant to the 150 l reactor. By evaluating certain mixing characteristics like the mixing time, k_1a -value, holdup, power input and shear rate it can be seen from the simulations that the current code has certain limitations which are described and solved throughout this thesis.

These limitations are found in the conversion factors for LBM, the boundary handling of the species model, the coupling force from gas phase onto fluid phase in the species calculation, the parcel approach described in the previous chapter as well as the mass transfer calculation from gas phase to fluid phase.

The simulation should be able to predict the quantities in a wide range of operating conditions and for different reactor scales and is therefore compared with measured data on a lab scale 150 l reactor and with empirical correlations.

Chapter 2

Scale-Up Strategies

2.1 Scale-Up parameters

2.1.1 Mixing Time

When a substance is introduced into a stirred tank the uniformity of the mass distribution increases with time up to an equilibrium concentration. By measuring mean concentrations in certain areas of the vessel an exponential decay or and a certain amount of oscillations in the concentration over time can be seen, depending on the position of the measuring point. The mixing time is therefore defined as the time it takes until the variation in concentration is within a certain intervall. In our cases the mixing times t_{90} , t_{95} and t_{99} are compared which correspond to the time it takes for the variation to be within 10%, 5% and 1% around the equilibrium value.

The concentration values are normalized, so that the equilibrium value equals 1[10, p. 172].

$$c'_i = \frac{c_i - c_0}{c_\infty - c_0} \quad (2.1)$$

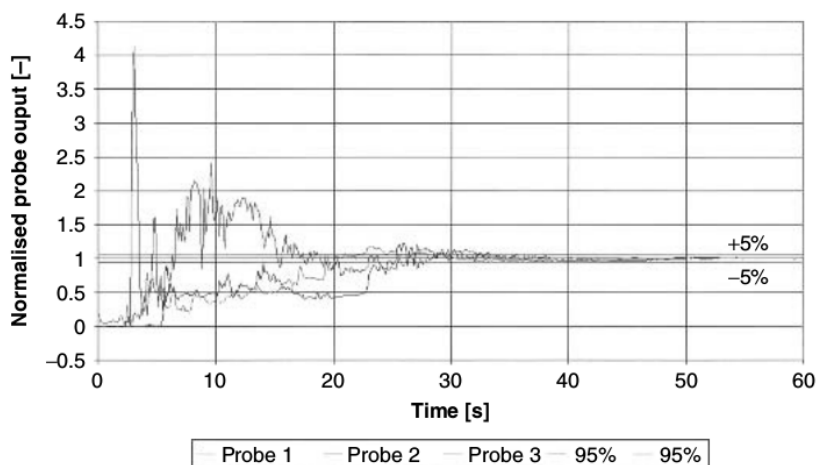


Figure 2.1: Example of normalized conductivity probe responses[10, p. 173]

In figure 2.1 an example of a normalized concentration curve over time is shown, where the values have been obtained by a conductivity measurement on three different sampling points [10, p. 173].

In the simulations in this thesis the degree of mixedness is evaluated as the standard deviation of the concentrations in each calculation cell. With this method the mixing quality is calculated based on the whole reactor domain.

$$\bar{c} = \frac{1}{n} \sum c_i \quad (2.2)$$

$$s = \sqrt{\frac{\sum |c_i - \bar{c}|^2}{n}} \quad (2.3)$$

\bar{c} denotes the mean concentration over the whole reactor, c_i is the concentration in each cell, n is the number of cells and s is the standard deviation. The standard deviation will decay to an equilibrium value that is not zero because the solid wall nodes are not taken out from the calculation. This decay behaves in a similar manner to the concentration profile as we will see later, therefore the mixing times can be evaluated in a similar manner.

2.1.2 k_1a -value

In a gassed stirred tank the dispersed phase leads to a mass transfer of gas into the liquid until the saturation equilibrium is reached. The equation describing the concentration c over time is given:

$$\frac{dc}{dt} = k_1a * (c^* - c) \quad (2.4)$$

Here c^* denotes the saturated concentration depending on the temperature and pressure. The volumetric mass transfer coefficient k_1a is specific to a given geometry and a given set of operating conditions. A higher k_1a -value leads to faster mass transfer.

Since the dissolution of gas is modeled in our simulations we can calculate the k_1a -value based on the resulting concentration profile over time. It combines the mass transfer coefficient k_1 and the specific surface area a of the dispersed phase over the reactor volume and is therefore given in s^{-1} .

2.1.3 Hold-Up

The amount of gas inside a stirred tank as well as the size distribution of the dispersed phase determine the interfacial area between gas and liquid. Since the mass transfer depends on this area, the gas holdup ϕ has a huge impact on the mass transfer. It is defined as the ratio of dispersed gas volume over the overall filling volume of the reactor and is given in percent.

$$\phi = \frac{V_G}{V_G + V_L} \quad (2.5)$$

2.1.4 Power Input

The power input needed to maintain the fluid motion is calculated in our simulations based on the energy dissipation ϵ at each calculation node. For gassed stirred tanks the power uptake can be significantly lower than for ungassed tanks, therefore the dissipation is multiplied by $(1 - \phi_{local})$ at each lattice node to account for the bubble volume. The dissipation is then integrated over the whole reactor domain [4].

$$P = \int_V \rho \epsilon dV \quad (2.6)$$

2.1.5 Shear rate

The shear rate is an important parameter in cell culture bioreactors because microorganisms tend to be very sensitive to mechanical stress. If the shear rate exceeds a certain critical value these microorganisms can break up and are therefore no longer available for the biological process. The shear rate is calculated with the already implemented model listed in chapter 1.4.

2.2 Dimensional analysis

By scaling the geometry of a stirred tank, full similarity of all quantities can not be achieved. In this chapter the dependency of the process parameters on a geometrical scale up factor is examined.

Either the volumetric power input P/V , the stirrer speed N , the blade tip velocity U_{tip} or the Reynolds number is kept constant and the remaining parameters are compared.

Constant volumetric power input

By setting a constant P/V , which corresponds to the average energy dissipation ϵ_{avg} , we can compute the necessary stirrer speed for the upscaled process:

$$\epsilon_{avg} = \frac{P}{V} \quad (2.7)$$

As we have seen earlier, the power input can be calculated from the dimensionless power number:

$$P = N_p * \rho N^3 D^5 \quad (2.8)$$

By setting $\epsilon_1 = \epsilon_2$ we get:

$$\frac{N_p * \rho N_1^3 D_1^5}{V_1} = \frac{N_p * \rho N_2^3 D_2^5}{V_2} \quad (2.9)$$

The density ρ is constant as well as N_p in the turbulent regime in which the simulations are done. With geometric similarity the volume can be represented by the reactor diameter $V \sim D^3$.

The stirrer speed for the upscaled process can now be expressed:

$$\frac{N_2}{N_1} = \left(\frac{D_2}{D_1}\right)^{-2/3} \quad (2.10)$$

Comparing the Reynolds number $Re = ND^2/\nu$ yields:

$$\frac{Re_2}{Re_1} = \left(\frac{D_2}{D_1}\right)^{4/3} \quad (2.11)$$

and for the tip speed $U_{tip} = D\pi N$:

$$\frac{U_{tip,2}}{U_{tip,1}} = \left(\frac{D_2}{D_1}\right)^{1/3} \quad (2.12)$$

Constant stirrer speed

In a similar manner the stirrer speed N can be kept constant whereas the volumetric power input is now calculated.

$$\frac{\epsilon_2}{\epsilon_1} = \left(\frac{D_2}{D_1}\right)^2 \quad (2.13)$$

$$\frac{Re_2}{Re_1} = \left(\frac{D_2}{D_1}\right)^2 \quad (2.14)$$

$$\frac{U_{tip,2}}{U_{tip,1}} = \left(\frac{D_2}{D_1}\right) \quad (2.15)$$

Constant tip velocity

By setting the tip velocity U_{tip} constant following relations are obtained:

$$\frac{N_2}{N_1} = \left(\frac{D_2}{D_1}\right)^{-1} \quad (2.16)$$

$$\frac{\epsilon_2}{\epsilon_1} = \left(\frac{D_2}{D_1}\right)^{-1} \quad (2.17)$$

$$\frac{Re_2}{Re_1} = \left(\frac{D_2}{D_1}\right) \quad (2.18)$$

Constant Reynolds number

The effect on the scale-up by setting a constant Reynolds number yields:

$$\frac{N_2}{N_1} = \left(\frac{D_2}{D_1}\right)^{-2} \quad (2.19)$$

$$\frac{\epsilon_2}{\epsilon_1} = \left(\frac{D_2}{D_1}\right)^{-4} \quad (2.20)$$

$$\frac{U_{tip,2}}{U_{tip,1}} = \left(\frac{D_2}{D_1}\right)^{-1} \quad (2.21)$$

The relations for a constant Reynolds number show very low stirrer speeds and volumetric power input. The mixing characteristics of such a process would be significantly worse than for the unscaled device and therefore this scale-up approach is not further investigated.

2.3 Correlations

Mixing time

Fasano et. al. [5] postulated a correlation for the mixing time with respect to a given uniformity U :

$$t_{m,u} = \frac{-\ln(1-U)}{k_m} \quad (2.22)$$

k_m is a mixing-rate constant that is specific to a certain stirrer geometry. For a six-bladed disc like the rushton turbine it can be calculated as follows:

$$k_m = aN \left[\frac{D}{T} \right]^b \left[\frac{T}{Z} \right]^{0.5} \quad (2.23)$$

with D being the impeller diameter, N the stirrer speed, T the tank diameter, Z is the liquid level in the reactor, a and b are constants which equal to 1.06 and 2.17 respectively.

If the mixing time for a given mixing quality of a stirred tank is known, the times for different mixing qualities can be estimated by a simple correlation given in the Handbook of Industrial Mixing [10, p. 173]

$$\frac{t_{m,u2}}{t_{m,u1}} = \frac{\ln(1-u_2/100)}{\ln(1-u_1/100)} \quad (2.24)$$

t_n stands for the mixing time for a given mixing quality n in percent.

A rough approximation is given by Kawase et. al. [7]:

$$t_{m,95} = 42.7/N \quad (2.25)$$

k_1a -value

The k_1a -value is calculated from measured oxygen saturation curves in the lab scale 150 l reactor with different operating parameters. From this data an expression of the following form is fitted to the measurements:

$$k_1a = a * \left(\frac{N^2D}{g}\right)^b * \left(\frac{Q}{ND^3}\right)^c \quad (2.26)$$

where the dimensionless Froude number $Fr = \frac{N^2D}{g}$ and Flow number $Fl = \frac{Q}{ND^3}$ are fitted with the exponents a, b, c .

Above equation was fitted to the experimental data within a range of $0.147 < Fr < 0.986$ and $0.02 < Fl < 0.492$:

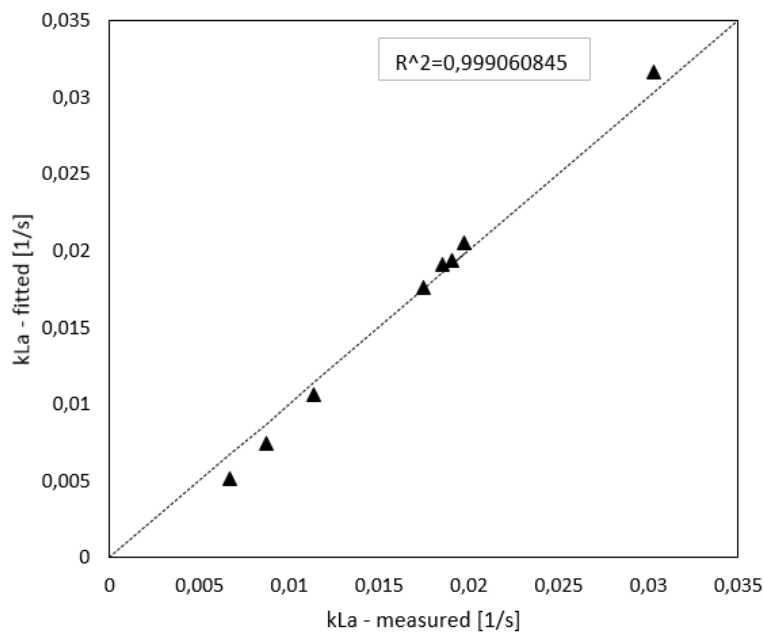


Figure 2.2: Regression model of the measured mass transfer data

The fitted parameters lead to the following equation:

$$k_1a = 0.07677 * \left(\frac{N^2D}{g}\right)^{0.6455} * \left(\frac{Q}{ND^3}\right)^{0.31886} \quad (2.27)$$

Several dimensionless correlations for the k_{La} -value can be found in published literature. For the small scale reactor no experimental data is available, therefore the following equations are used for comparison with the simulations:

$$\frac{k_{La}T^2}{D_L} = 21.2 \left(\frac{\rho NT^2}{\mu_a} \right)^{1.11} \left(\frac{\mu_a}{\rho D_L} \right)^{0.5} \left(\frac{U_s T}{\sigma} \right)^{0.45} \left(\frac{\mu_G}{\mu_a} \right)^{0.69} \quad (2.28)$$

Above equation is postulated by Perez et. al. [11] and is valid for stirred tanks. However the simulations on the small scale reactor are tested with very low stirrer speeds, therefore the reactor acts as a bubble column. A correlation for the k_{La} value for bubble columns is given by Akita et. al. [1]:

$$\frac{k_{La}T^2}{D_L} = 0.6 \left(\frac{D^2 \rho g}{\sigma} \right)^{0.62} \left(\frac{D^3 \rho^2 g}{\mu^2} \right)^{0.3} \left(\frac{\mu}{\rho D_L} \right)^{0.5} \phi^{1.1} \quad (2.29)$$

A correlation for Non-Newtonian fluids is proposed by Costa et. al. [3] and is valid for stirred tanks with power law fluids:

$$\frac{k_{La}T^2}{D_L} = 8.38 \left(\frac{\rho N^{2-n} T^2}{\mu} \right)^{2/3} \left(\frac{K}{\rho N^{1-n} D_L} \right)^{1/3} \left(\frac{\rho N^2 T^3}{\sigma} \right)^{0.43} \left(\frac{NT}{U_s} \right)^{-0.3} \left(\frac{T}{D} \right) \left[1 + 1.5 * 10^{-3} \frac{\rho N^2 T^3}{\sigma} \right] \quad (2.30)$$

Hold-up

The same procedure as for the k_1a -value is carried out for the measured holdup data. The postulated correlation is also based on Froude number and Flow number:

$$\phi = a * \left(\frac{N^2 D}{g} \right)^b * \left(\frac{Q}{ND^3} \right)^c \quad (2.31)$$

The measurements are made in a range from $0.156 < Fr < 1.026$ and $0.019 < Fl < 0.125$.

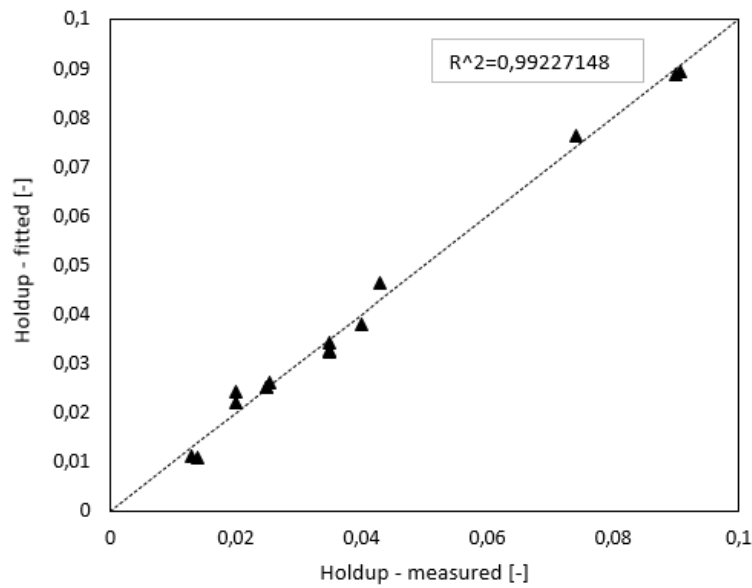


Figure 2.3: Regression model of the measured holdup data

Following equation is obtained:

$$\phi = 0.5933 * \left(\frac{N^2 D}{g} \right)^{0.5966} * \left(\frac{Q}{ND^3} \right)^{0.7229} \quad (2.32)$$

Power input

The power input is calculated as described and is given in W . In order to make it comparable between different vessel sizes it can be made dimensionless to yield the Newton number:

$$N_p = \frac{P}{\rho N^3 D^5} \quad (2.33)$$

This dimensionless number is calculated and compared for all our simulations. For sufficiently large Reynolds numbers this Newton number stays constant as it is seen in figure 2.4.

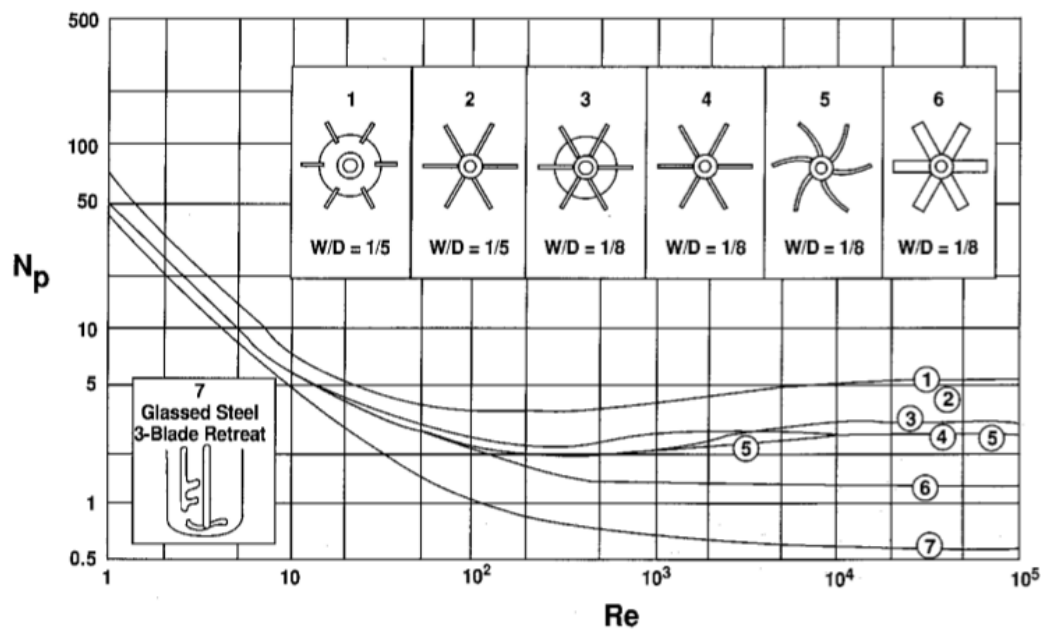


Figure 2.4: Newton number over Reynolds number [10, p. 361]

In the handbook of industrial mixing [10, p. 361] there are several correlations in order to correct the turbulent Newton number for different blade sizes. For a Rushton turbine with the geometry of the 150 l reactor the Newton number is calculated to be 7.9 for a single stirrer. For a triple Rushton turbine with sufficiently large clearance between each impeller this Newton number can be multiplied by the number of impellers. The Power number for the 150 l and 19.29 m^3 reactor is therefore 23.7.

Shear rate

Two general relations for the shear rate inside a stirred tank reactor are compared. The first one is proposed by Wichterle et. al. [21] and predicts the maximum shear rate that occurs inside the reactor:

$$\dot{\gamma}_{max} = N(1 + 5,3n)^{1/n} \left(\frac{N^{2-n} d_i^2 \rho}{K} \right)^{1/(1+n)} \quad (2.34)$$

Secondly the average shear is evaluated. The most general form for the average shear rate is postulated by Perez et. al. [12]:

$$\dot{\gamma}_{avg} = \left(\frac{4N_p \rho d_i^2}{\pi 27K} \right)^{1/(1+n)} N^{3/(1+n)} \quad (2.35)$$

Chapter 3

Internal Tank Geometries

In this chapter the implementation of several tank internals is described. In order to accurately obtain the fluid flow field it is necessary to capture details on the top of the reactor like sensors reaching into the fluid region. A major influence on the fluid flow results from heat exchanger bundles that are placed inside the vessel. A new stirrer type, the so called elephant ear impeller, is implemented next to the already available standard Rushton turbine.

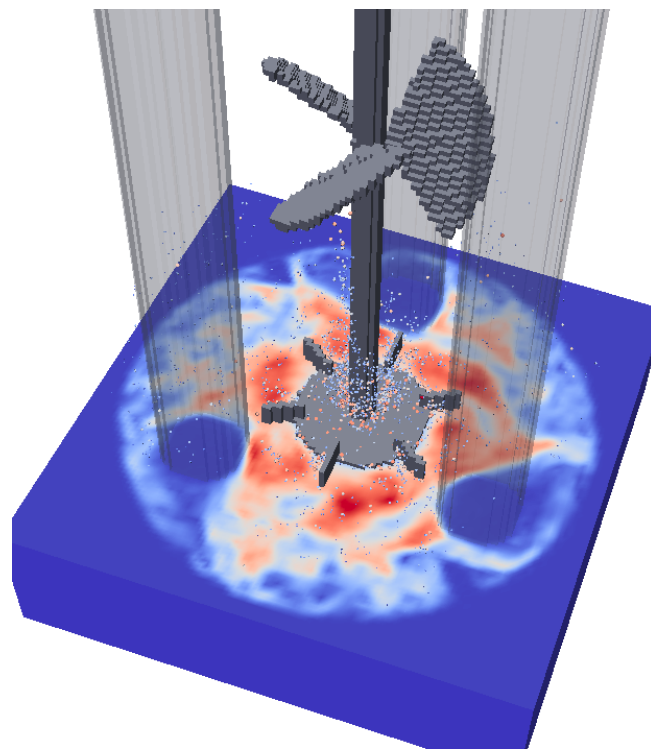


Figure 3.1: Reactor with bottom Rushton turbine and top elephant ear impeller

In figure 3.1 a setup of a reactor with a Rushton turbine at the bottom, an elephant ear impeller on top and heat exchanger bundles is shown.

3.1 Stirrer geometries

For the simulation of different kinds of reactors the standard Rushton turbine is used, as well as the elephant-ear impeller.

These elephant-ear impellers allow for larger axial pumping due to the pitched blades. The geometry is described by the parameters given in table 3.1.

Table 3.1: Elephant-ear impeller parameters

<i>Parameter</i>	<i>Unit</i>	<i>Description</i>
Blade outer diameter	[m]	The outermost diameter of the stirrer geometry
Blade inner diameter	[m]	The inner diameter where the wedged blades start
Disk diameter	[m]	Outer diameter of the disk onto which the blades are mounted
Blade angle	[°]	The angle at which the blades are tilted from the z-axis
Blade spread angle	[°]	The angle that each wedge is spread out from the mounting point on the disc (cut-out angle)
Blade number	[-]	Number of wedge blades equally distributed along the circumference

The geometry of the elephant ear impeller is implemented by looping through the z coordinate, the radial coordinate and the bladenumber. If a calculation node is near the theoretical stirrer geometry, based on the impeller parameters, it is marked as solid.

For the solid interaction with the gas bubbles the normal vectors at the boundary nodes on the stirrer are needed. They are calculated and stored everytime a stirrer node is marked as solid.

3.2 Heat exchanger

In order to simulate the flow around bundles of small tubes the resolution of the uniform grid would have to be fine enough to describe the geometry and curvature of these tubes. This resolution is much higher than the resolution needed for the rest of the reactor. In our simulations the cell size can be as large as a single tube. Therefore the tubes are not defined as solid walls within the fluid regions but are treated as a porous medium with a defined solid fraction.

In Figure 3.2 the actual heat exchanger tubes are shown on top of a typical lattice. It can be seen that the resolution is not sufficient for a direct simulation of the fluid flow around these tubes. A solid fraction between 0 and 1 is now set in the region of the tube bundle. The value is set to the fraction of the tube volume over the overall volume inside the bundle diameter.

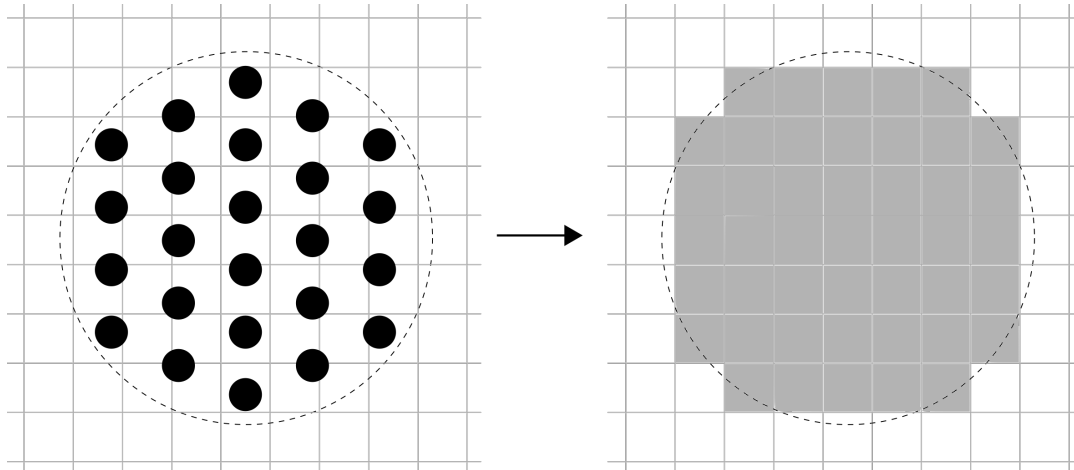


Figure 3.2: Grid adaption for the heat exchanger model

The macroscopic porous media model is implemented by adding an additional term after the usual collision and streaming step in the LBM, as it is described by Sukop et. al. [15]. If a node has a solid fraction of 0 the flow is undisturbed and is handled as usual. If the solid fraction is larger than 0 then a part of each distribution function is reflected. The solid fraction can be viewed as a bounce-back probability.

$$f_i(\mathbf{x}, t+1) = f_i^{coll}(\mathbf{x}, t+1) + n_S(\mathbf{x}) \left[\tilde{f}_i^{coll}(\mathbf{x}, t+1) - f_i^{coll}(\mathbf{x}, t+1) \right] \quad (3.1)$$

In equation 3.1 the porous bounce-back step is shown, where f_i values are corrected after the collision step and streaming step. $n_S(\mathbf{x})$ is the solid fraction, and \tilde{f}_i is the distribution function in the opposite direction of the current vector. It can be seen that for a solid fraction of 1, the f_i value becomes the value of the opposite vector and is therefore fully bounced back.

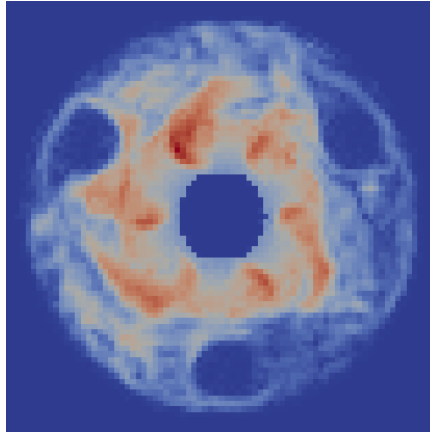


Figure 3.3: Heat exchanger model - top view of the flow field

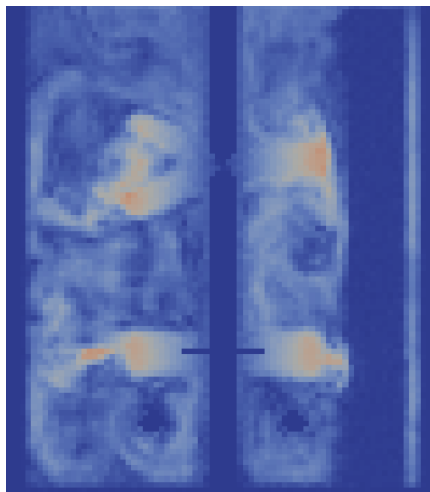


Figure 3.4: Heat exchanger model - side view of the flow field

In the above figures, an example of a setup with heat exchanger geometry is shown inside the small scale 20 Liter reactor. The bundles have been initialised with $n_s = 0.01$

3.3 Sensors

Inside the reactor certain small internal geometries can be present which also influence the fluid motion. Most of these geometries are usually sensors which reach into the fluid region from the top of the reactor. These sensors are now implemented in the simulation code.

Multiple sensors can now be specified on a certain radius and with individual diameters and lengths. The parameters are given in table 3.2.

Table 3.2: Sensor parameters

<i>Parameter</i>	<i>Unit</i>	<i>Description</i>
Sensor	[true/false]	Activating/Deactivating the sensor geometry
Circle diameter	[m]	Diameter of the circle on which the sensors lie.
Angle	[°]	Angle at which the sensor lies on the xy-plane starting from the x-axis
Bottom height	[m]	Clearance from the reactor bottom to the sensor
Diameter	[m]	Diameter of the sensor itself

A visual representation of the parameters is shown in the following figures.

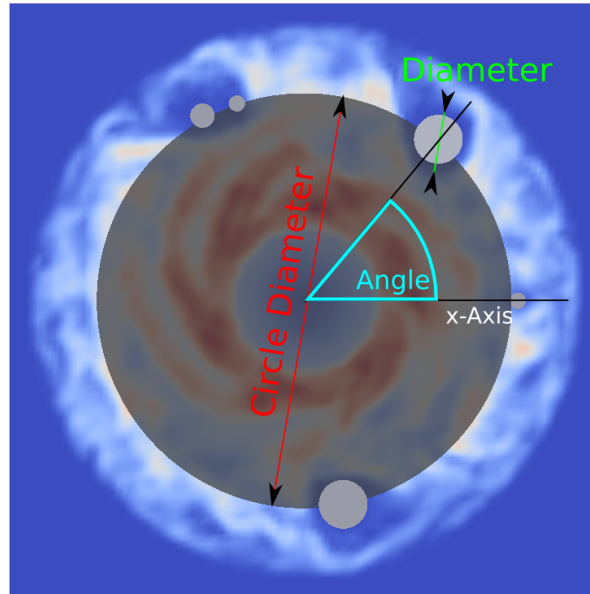


Figure 3.5: Sensor parameters - top view

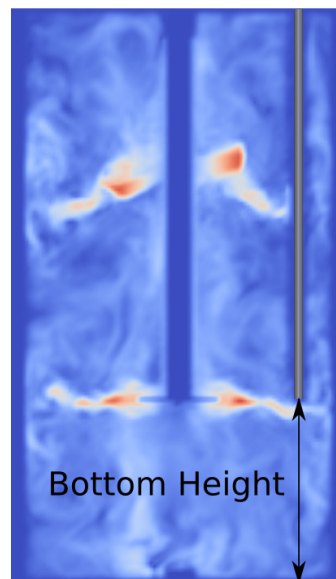


Figure 3.6: Sensor parameters - side view

Chapter 4

Species Transport

4.1 Initialisation

The introduction of substrate into a reactor is either performed by an initial amount of this substrate at a certain position (e.g. feed tube outlet) at the beginning or by adding small amounts of substrate throughout the process, as it is usually done in fed-batch reactors. Gases can also be transferred from the bubbles to the liquid phase.

In our simulations pulses of substrate are introduced during a short amount of time (e.g. 1 second) in order to measure the mixing time afterwards. The following parameters can be adjusted for the initialisation of substrate:

Table 4.1: Species initialisation parameters

<i>Parameter</i>	<i>Unit</i>	<i>Description</i>
Discharge rate	[kg/h]	Mass of substrate per hour that is introduced into the reactor
Discharge concentration	[kg/kg]	Mass loading of the substrate solution
Discharge amount	[kg]	Total mass of substrate discharged
Discharge start time	[s]	Time at which the discharge starts

4.2 Boundary handling

As stated in the introduction the species transport in the fluid region yields good results for the mixing characteristics, but at the boundary the bounce-back condition in the streaming step can lead to instabilities. These instabilities are due to the complex geometry of the reactor internals which are approximated by a uniform grid in our simulations. The concentration in some boundary cells can get higher than the surrounding region would allow, although the global mass is conserved. This means that a form of de-mixing can occur at boundary nodes especially in the corners where the D3Q27 vectors, which always represent a certain amount of mass, can be reflected back and forth inside one single node.

To reduce this problem a free-slip condition is applied. On the boundary nodes the vectors are then not just reflected onto the opposite vector but onto the vector that is reflected off of the wall like shown in figure 4.1.

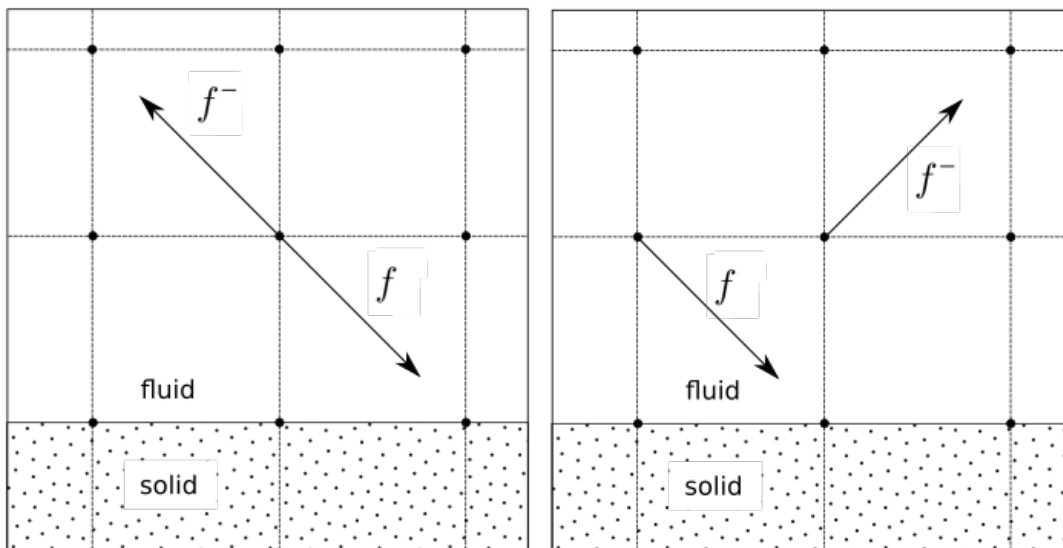


Figure 4.1: Bounce-back and free-slip condition

In order to further reduce de-mixing effects that still occur with the free-slip condition, an additional diffusion is introduced at the boundary nodes. This means the velocity vectors of the species transport at these nodes are not given by the fluid velocity, but the species mass is distributed in every direction of the D3Q27-lattice. The species vector is then purely given by each corresponding weighting factor w_i and the local species mass m_i , whereas $\sum w_i = 1$:

$$f_i = w_i * m_i \quad (4.1)$$

4.3 Gas-Phase coupling

As stated in the introduction the fluid and gas phase are coupled, where the gas phase influence onto the fluid field is given by a local force. This local force is able to predict the effect of the bubbles on the fluid velocity and should therefore be able to predict the effect on the macroscopic mixing of a dispersed substance in the reactor. By simulating a series of operating conditions with the small reactor at 20 rpm, following results have been obtained for the mixing time t_{95} :

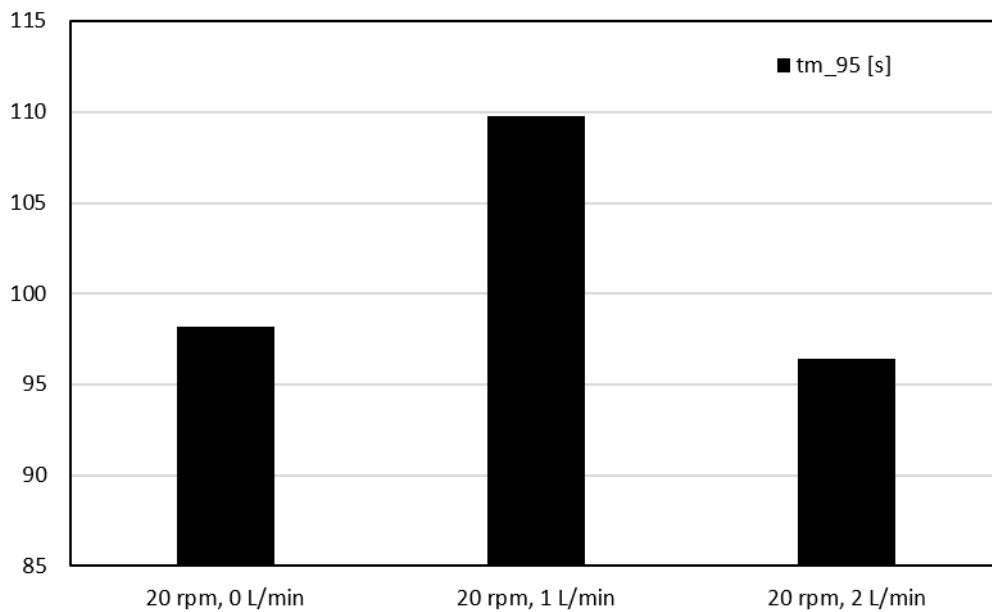


Figure 4.2: Mixing times in the 20 Liter reactor

The trend for increased gassing rates shows inconsistent mixing times. The expected mixing times would decrease with increased gassing rate. The consideration of local coupling force between gas and fluid phase results in unphysical mixing behaviour in the species transport model in the present form.

The effect of the coupling force in the species kernel is now varied: Rather than increasing the velocity by the amount of the coupling force, this coupling force is now subtracted.

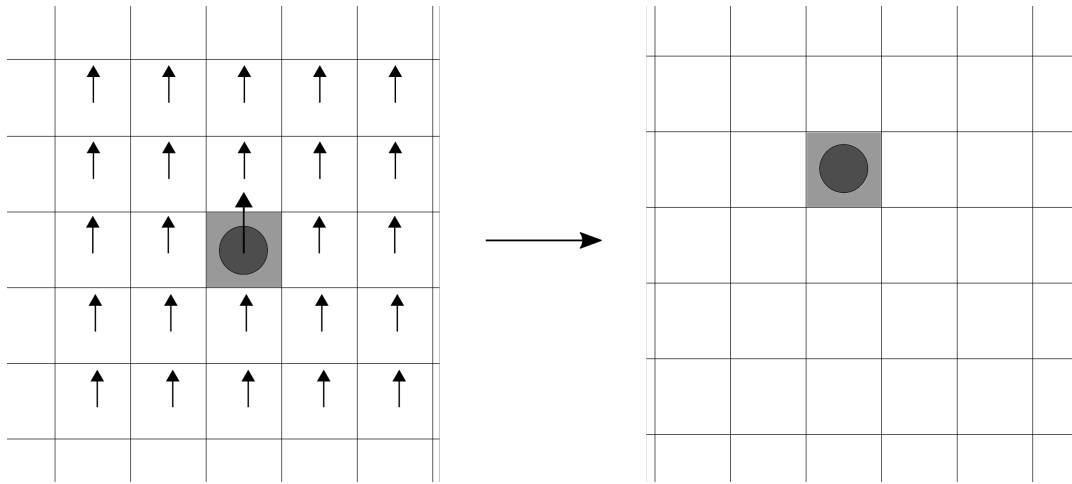


Figure 4.3: Gas phase coupling with added coupling force

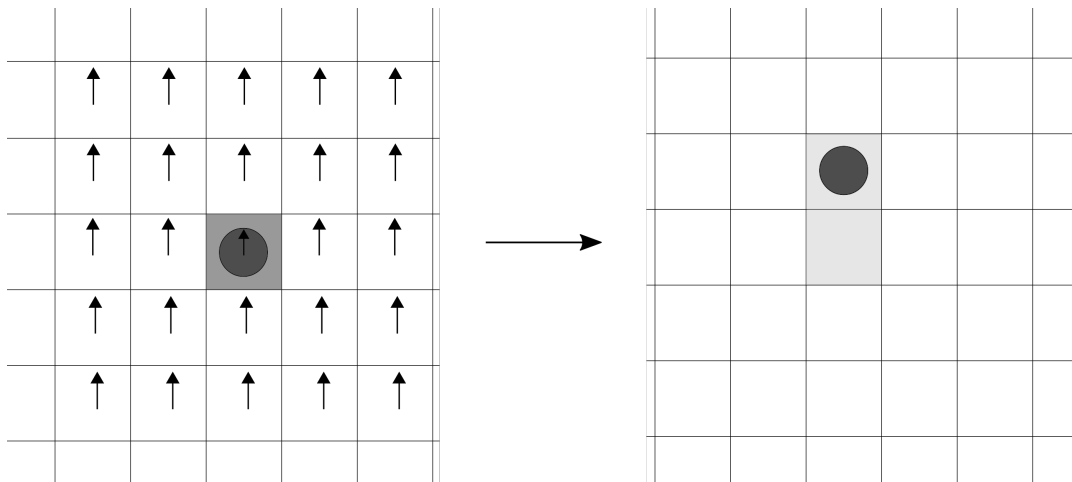


Figure 4.4: Gas phase coupling with subtracted coupling force

In figure 4.3 the species transport with the added coupling force is shown. A bubble resides on the node with a certain mass of species within the velocity field. Because of the high velocity all the species mass is convected towards the upper node. In figure 4.4 the species transport velocity is smaller than the fluid flow, therefore only part of the species is convected while the rest is residing on the first node. Due to this back-mixing effect the standard deviation of the concentration decreases faster, resulting in lower mixing times for higher gassing rates.

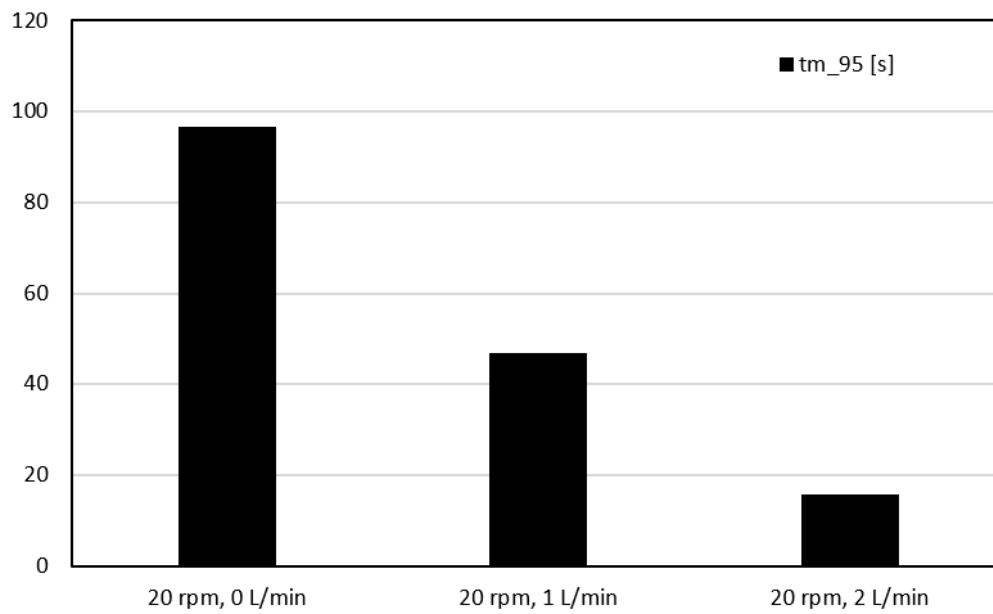


Figure 4.5: Mixing times in the 20 Liter reactor - new gas phase coupling

In figure 4.5 the new simulation results are shown. The mixing times now follow a clear trend towards lower mixing times for higher gassing rates. It is worth to note here that another correction is made in the lattice units, which is described in the next chapter.

4.4 Calculation of mass transfer

The following relation for the transferred mass is already described in the introduction.

$$\Delta m = k_l * A * (c^* - c) * MW_{O_2} * \Delta t \quad (4.2)$$

The overall mass that is present in the reactor is calculated at certain time steps by summing up the oxygen mass in each calculation call and is plotted over time. With the concentration of oxygen over time the k_1a -value can be calculated.

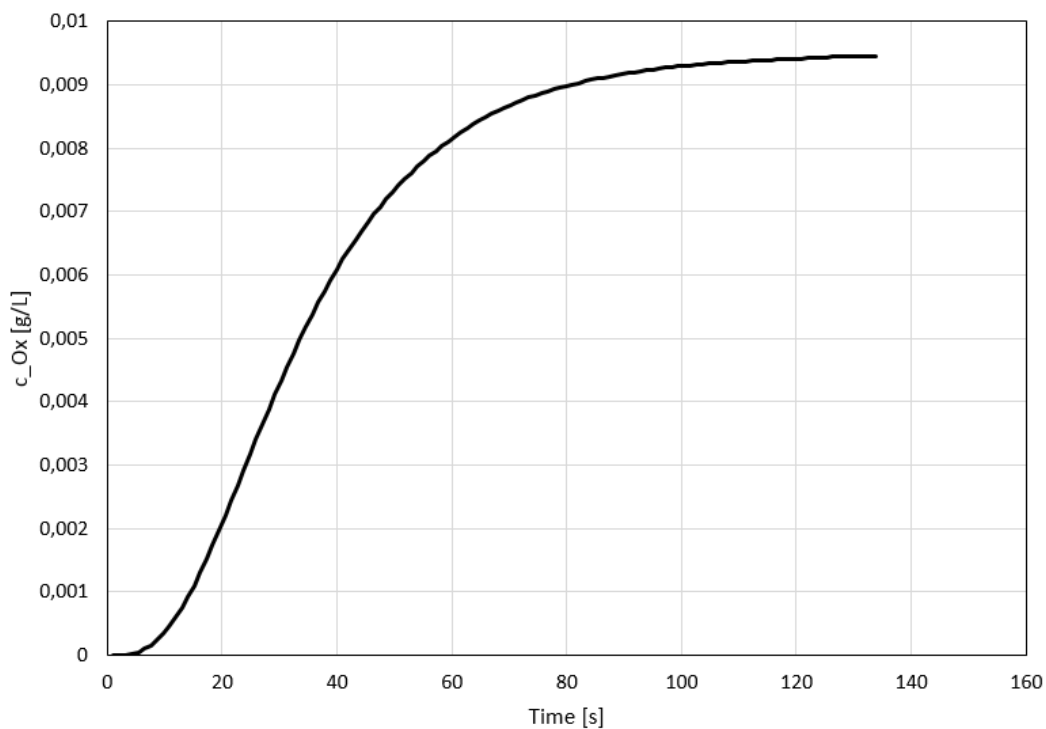


Figure 4.6: Simulated oxygen concentration over time

In figure 4.6 an example for a oxygen concentration term obtained in a simulation of the large scale reactor is shown. The corresponding k_1a -values show inconsistent results, e.g. higher gassing rates can lead to lower values and they also show no correlation with empirical correlations that are compared.

The mass transfer is now modified in order to overcome this bias: The time step Δt in Equation 4.2 is now decreased. In the existing gas phase model, 5 bubble time steps are performed during 1 fluid calculation step. In every bubble step the boundary conditions for the bubble movement, e.g. reflection at the walls, are applied. Therefore the bubble movement is described more accurately than with the fluid timestep.

The transferred mass is now obtained in each bubble step. So the time Δt is only a fifth of the fluid calculation time step. Finally the values for mass transfer are copied to the species transport model which then adds the oxygen mass onto each cell.

The mass transfer model is visualised in figure 4.7. The bubble can pass several fluid cells during the bubble steps. If only position 0 and 5 is considered, all the oxygen mass in the path in between would not be resolved. By considering the bubble positions at each bubble step the concentration profile is shown to be more accurate.

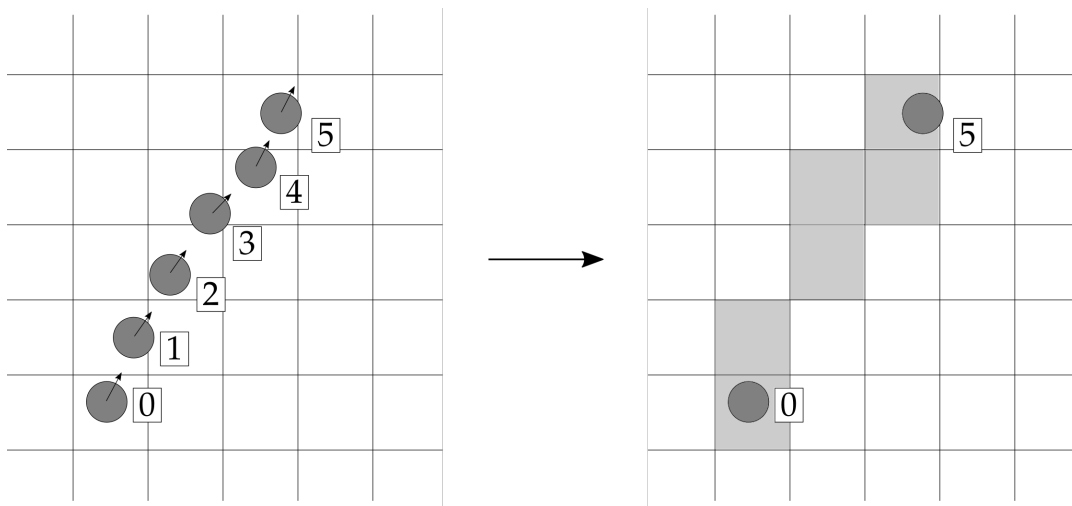


Figure 4.7: Mass transfer from gas phase to fluid phase

Chapter 5

Simulation improvements

5.1 Lattice unit correction

The choice of lattice units is described in the introduction. This unit conversion is crucial for the numerical stability and accuracy of the LBM procedure. One important criteria is the limitation for low Mach-numbers. This means that the ratio of the highest velocity inside the whole domain and the speed of sound shall be no larger than a certain value.

Usually the highest velocities occur at the tip of the stirrer blades, therefore the tip speed is set to 0.01 in lattice units. For small rotational speeds this tip speed can be lower than the rising velocity of the bubbles initialised at the gas sparger. This means that the speed limit can not be guaranteed anymore.

In order to overcome this instability an estimation for the bubble rising velocity, based on the bubble diameter, is implemented. If this velocity is larger than the blade tip speed, the LBM conversion factor for time is calculated based on this estimation.

The estimation is based on the correlations from Talaia [17] and is given by the following equations for the bubble velocity:

$$u_b = \begin{cases} 1.545 \left(\frac{gd\Delta\rho}{\rho_l} \right)^{0.5} & , 1.4mm < d < 3.1mm \\ \left(0.289 \frac{gd\Delta\rho}{\rho_l} + 877.193 \frac{\mu_l g^{0.5}}{\rho_l d^{0.5}} \right)^{0.5} & , 3.1mm < d < 13.4mm \\ 0.714 \left(\frac{gd\Delta\rho}{\rho_l} \right)^{0.5} & , 13.4mm < d < 22.8mm \end{cases} \quad (5.1)$$

5.2 Parcel approach stability

As it is stated in the introduction a parcel approach is implemented in the gas phase model of the simulation. This allows for a high number of simulated gas bubbles because multiple bubbles are represented by a single lagrangian particle. This approach shows consistent results but must be initialised correctly.

Throughout the simulation the gas phase volume is calculated for each fluid node. If a certain calculation cell contains too many bubbles the gas phase volume becomes larger than the actual volume of the calculation cell itself. If this happens the bubbles are repeatedly displaced by a small amount until the bubble volume is consistent with the cell volume again. This displacement is modeled by introducing a small random velocity vector, which is already implemented in the previous simulation code.

In this parcel approach the initial number of bubbles represented by one particle and the diameter of these, can be set in the input parameters. However if the volume represented by these initial parcels is larger than the cell volume, then this displacement vector described above is applied in every time step leading to random motion of the bubbles and unphysical bubble distribution results.

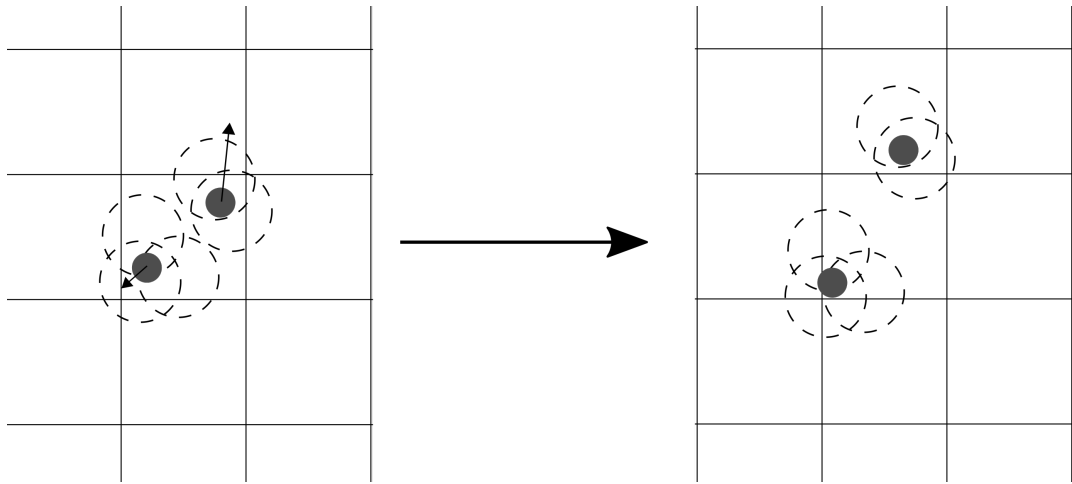


Figure 5.1: Bubble displacement for too high bubble volumes in a cell

In figure 5.1 the displacement of parcels is shown. Two parcels are present in the calculation cell, where each of the parcels have an individual bubble volume that is lower than the volume of the cell. If now both of these parcels happen to be located in the same cell, the bubble volume exceeds the cell volume and the random displacement vector is applied, resulting in the new parcel positions on the right. If now the bubble volume of a single parcel would be higher than the cell volume, then this displacement vector is always applied resulting in this unphysical behaviour.

This limitation is now considered in the simulation code and only allows for sufficiently small number of particles per parcel.

5.3 Serial simulation

In order to simplify the simulation of multiple reactors in series an automated routine has been developed. For this routine the input parameters must be given as *.JSON-files for each simulation. The files can be named arbitrarily but shall be unique and must not contain spaces. By starting the routine the first step is to detect all *.JSON-files in the simulation directory and then display them in a list. By confirming the selection a new file containing this simulation list is created with the name of each input file that has been selected for simulation. This is shown in figure 5.2, where WD denotes the current working directory.

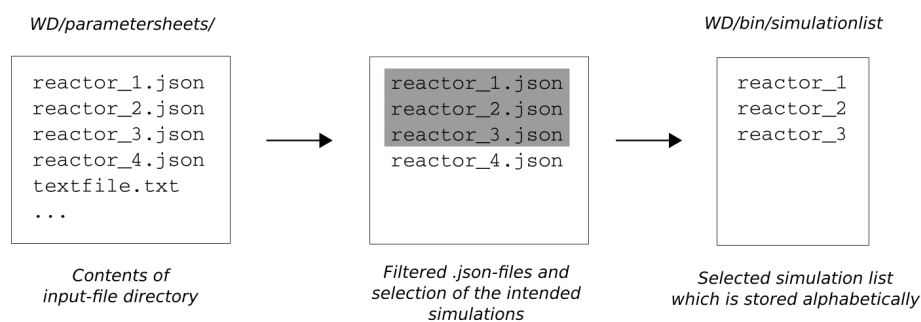


Figure 5.2: Start of a simulation series

Before starting the first simulation the directory is searched for any compiled version of the code. If there is no file the code is compiled as usual. Everytime the code is compiled an additional md5-checksum is created and stored that accounts for the current state of the source directory. If a compiled file already exists, then the md5-checksum of the current directory state and the one that is stored from the compilation process are compared. If they do not match the compilation process is started again. If they do match, then no changes have been made since the last compilation and the compiled version is used for the first simulation.

At the beginning of each individual simulation, all necessary files are stored in a directory named after the corresponding input file. This includes the input file itself and also the compiled version of the code. After that, the first simulation is started. When it is finished, the next input file is read in and a new directory with all the relevant files for the new simulation is created.

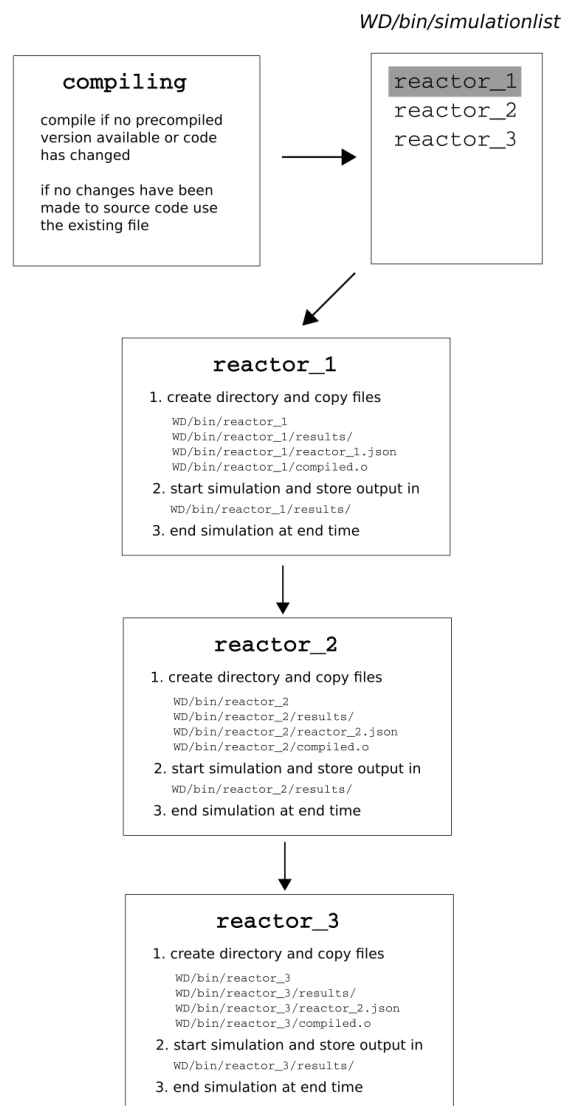


Figure 5.3: Compiling and running a simulation series

At certain points throughout each simulation, all the information located in the working memory at a certain time step is stored, which enables a restart of an interrupted simulation from this point. This restart routine is now adapted to the simulation series. When restarting a series of simulations, every directory of each individual simulation that has already been started or finished is searched for restart files. The names of directories containing such files are listed and stored. The names are ordered alphabetically, just like the simulation list that was created at the beginning of the simulation series. This means that the last entry of the restart list accounts to the newest simulation that has been interrupted. By starting the restart routine the simulation series is continued starting with the last entry of the restart list.

In figure 5.4 the restart routine for the simulation series example is shown, assuming that the simulation of the second reactor was interrupted.

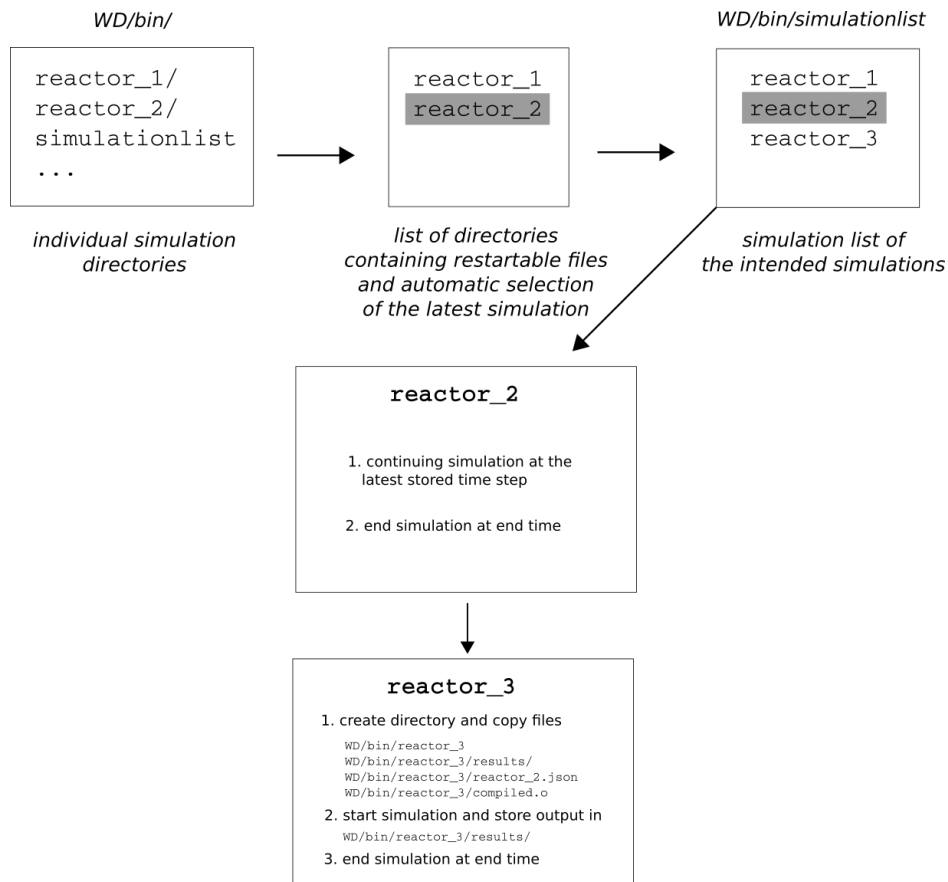
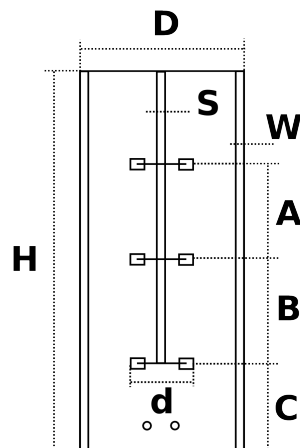


Figure 5.4: Restart routine for a simulation series

Chapter 6

Scale-Up Simulations

In this chapter the results from the scale-up simulations are discussed. The 150 l reactor as well as the 19 m³ reactor, with different scale up criteria, is simulated. The larger reactor is geometrically similar to the smaller reactor, but with a length based scale up factor of 5.



The following operating conditions have been tested:

Table 6.1: Scale up operating conditions

	150 l	19 m ³	19 m ³	19 m ³
Scale-Up criterion	-	$U_{tip} = const$	$P/V = const$	$N = const$
Stirrer speed [1/min]	275	55	94.05	275
Gas Flow Rate [m ³ /h]	0.4	10/50	10/50	10/50

Each scaled up process is simulated with 2 different gas flow rates. The lower gas flow results from a constant superficial gas velocity U_s , the higher gas flow is obtained by setting a constant volumetric gas flow $vvm = Q/V_{reactor}$. The notation of each process is given by the constant parameters.

Table 6.2: Froude number and Flow number for the Scale-Up simulations

	Fr	Fl
150 l	0.315	0.0076
$U_{tip} U_s$	0.063	0.0076
$U_{tip} vvm$	0.063	0.0382
$P/V U_s$	0.184	0.0045
$P/V vvm$	0.184	0.0223
$N U_s$	1.574	0.0015
$N vvm$	1.574	0.0076

The dimensionless Froude number and Flow number is given in table 6.2. Notice that not all of the obtained parameters are within the range of the regression model in chapter 2.

Due to the parcel approach, highly local effects like bubble swarms at the transition to the flooding regime are not captured. To ensure that none of these reactors is in the flooding regime the following relation is described by Paglianti [9]:

$$Fl_g = 30 \left(\frac{D}{T} \right)^{3.5} Fr \quad (6.1)$$

If the flow number exceeds Fl_g , then the reactor is operating in the flooding regime. The Flow numbers in the upscaled reactors are sufficiently small for all operating conditions in order to prevent flooding.

Table 6.3: Results of power input for the Scale-Up simulations

	P/V_{scaled}	$P/V_{simulated}$	N_p
150 l	-	925.37	21.70
$U_{tip} U_s$	185.07	186.66	21.79
$U_{tip} vvm$	185.07	183.01	21.37
$P/V U_s$	925.37	936.85	21.87
$P/V vvm$	925.37	906.92	21.78
$N U_s$	23134.25	25076.67	23.42
$N vvm$	23134.25	24285.43	22.68

In table 6.3 the dimensionless power numbers N_p obtained from the simulations, as well as the volumetric power input P/V , which is equal to the average dissipation rate ϵ inside the reactor, is compared to the scale up correlations in chapter 2.

The power numbers are in good agreement with the proposed literature value of 23.7. This value is valid for the ungasged power input, the power numbers from the simulations are slightly lower because of the gassing rate. It can be seen that higher gassing rates lead to lower power input.

6.1 Mixing times

The normalized mixing times for homogeneity of 90%, 95% and 99% are evaluated based on the standard deviation of the species concentration over time. The conversion between mixing times of different uniformity is calculated according to equation 2.24 and is based on the 95 % mixing time obtained in the simulations. The simulated values should then follow this curve. Also the correlation from Fasano et. al. [5] given by equation 2.22 is compared for different values of homogeneity and plotted over the simulated values.

The following curves have been obtained:

150 liter reactor

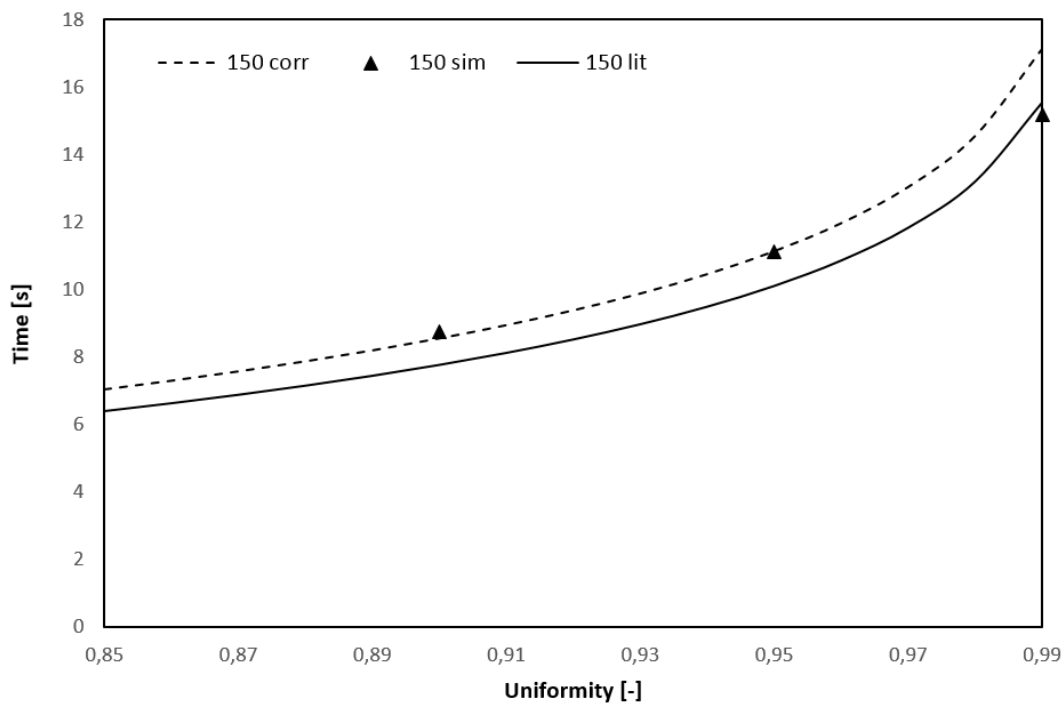


Figure 6.1: Mixing times for the 150 l Reactor

The dashed line is the curve of the conversion formula based on the 95 % mixing time, the solid line is the curve obtained from the correlation from Fasano and the points are the simulated values. Generally a good agreement between the mixing times were achieved. However the curve proposed by Fasano is slightly lower. The rough approximation with the correlation by [7] yields a mixing time of 6.484 s.

19 m³ reactor with constant U_{tip}

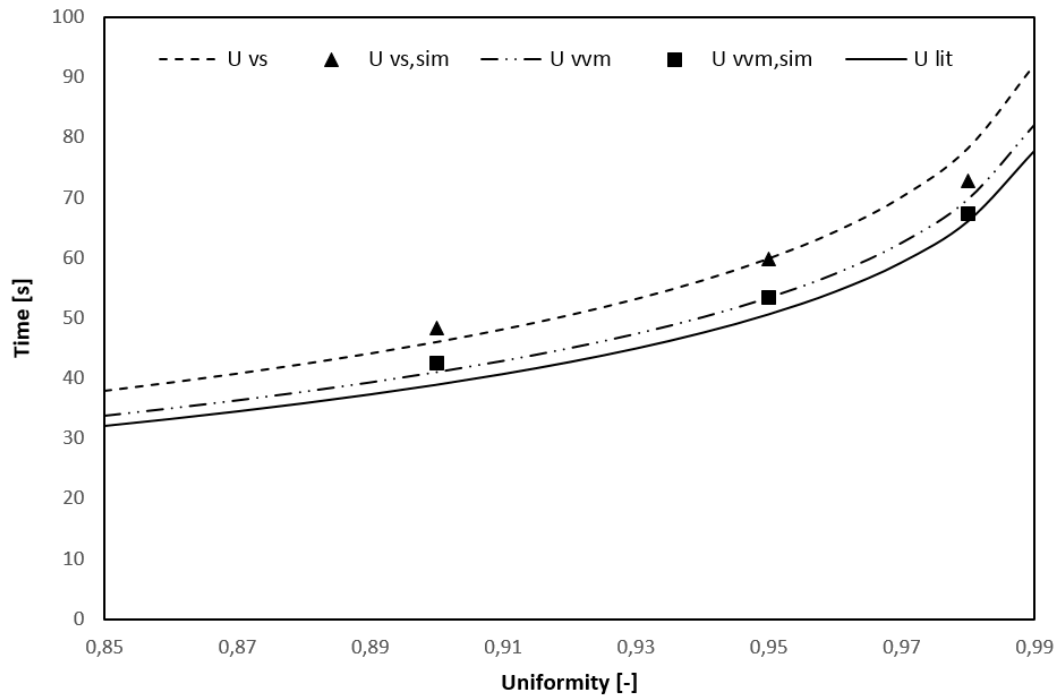


Figure 6.2: Mixing times for the 19 m³ Reactor with constant U_{tip}

For the upscaled reactor the mixing times for different operating conditions are compared. The additional dashed line stands for the higher gassing rate for a constant volumetric gas input vvm , the lower gassing rate is calculated by setting a constant superficial gas velocity U_s . Again the values are in good agreement and slightly higher than proposed by the literature correlation. The difference in gassing rate results in lower mixing times. The mixing time postulated by [7] is 46.58 s.

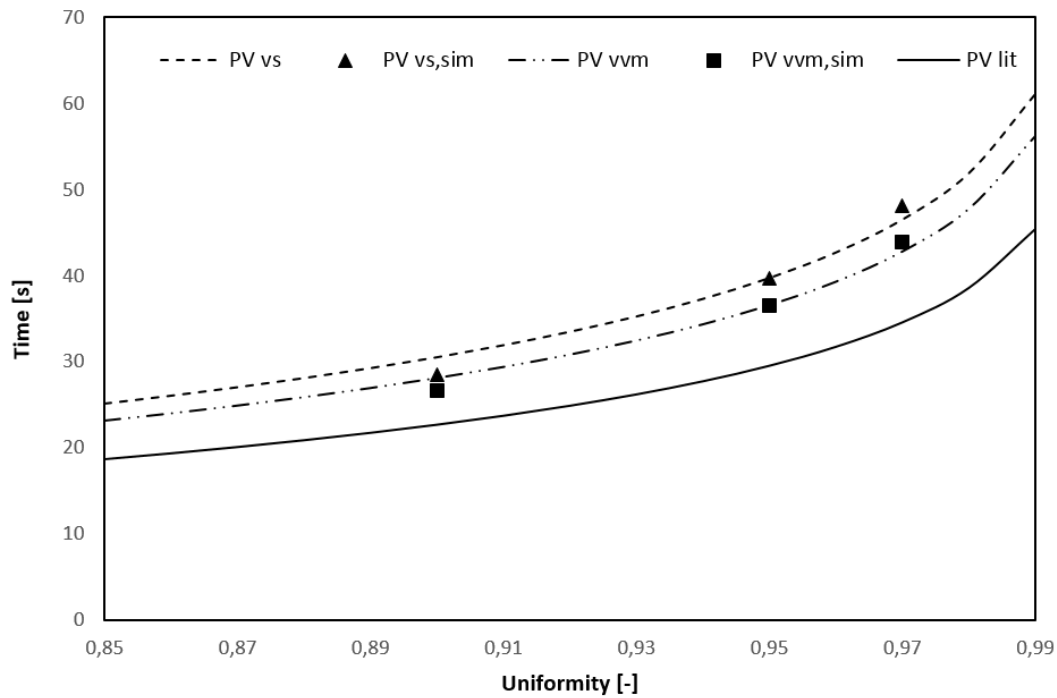
19 m³ reactor with constant P/V 

Figure 6.3: Mixing times for the 19 m³ Reactor with constant P/V

Also for the upscaled reactor with constant volumetric power input the mixing times correlation show the same trend. For this set of operating conditions however the deviation from the correlation from Fasano is larger, but the difference in gassed mixing times is clearly seen. For these operating conditions, the mixing time from the simple correlation from [7] leads to a value of 29.72 s which further validates the simulations and shows that the mixing times from Fasano underestimate the actual results.

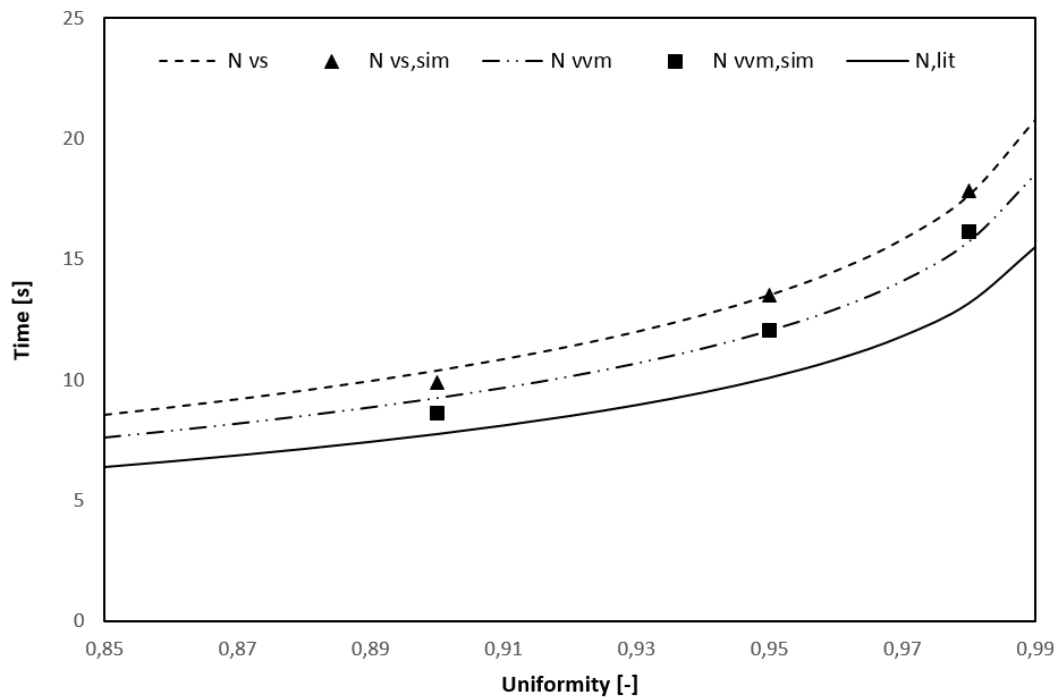
19 m³ reactor with constant N 

Figure 6.4: Mixing times for the 19 m³ Reactor with constant N

For a constant stirrer speed when upscaling from the 150 l reactor to the 19 m³ reactor, the mixing times again show good agreement. As expected, the difference in the mixing times for the different gassing rates is lower than for the lower stirrer speed at constant U_{tip} . Here, the correlation from Kawase [7] yields a 95 % mixing time of 6.483 s, the same as for the 150 l reactor.

6.2 k_{La} -value

From the simulated oxygen saturation curves over time, the k_{La} values are fitted and compared to the correlation proposed in chapter 2.

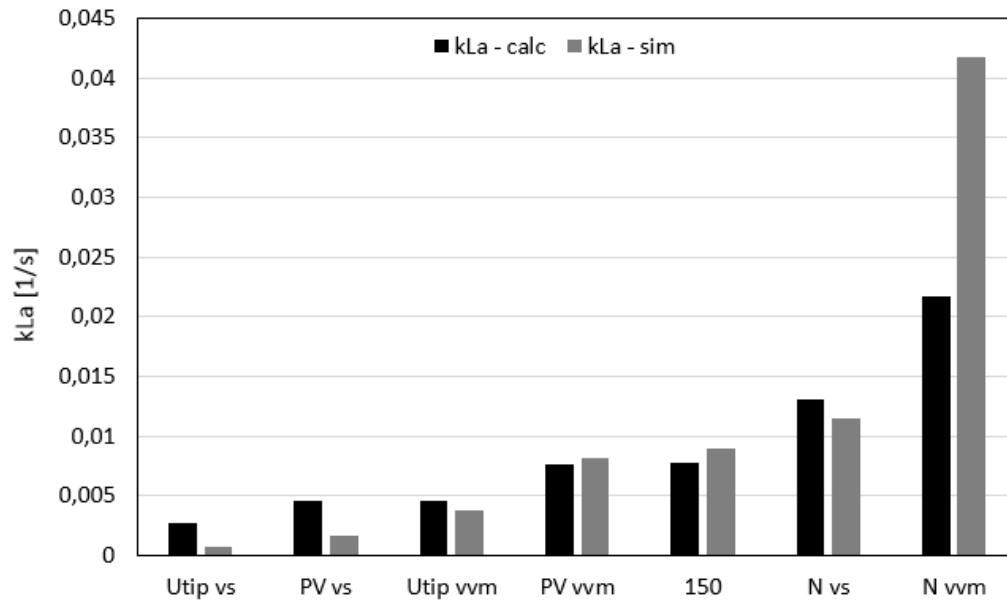


Figure 6.5: Comparison between k_{La} of simulation and model prediction

By comparing the Froude number and Flow number on the beginning of this chapter with the correlation proposed in chapter 2, it can be seen that only the scaled up reactor with constant P/V and vvm is within the given range of the correlation. However for the constant P/V U_s reactor and the constant U_{tip} vvm only one of the parameters is in the range.

In the medium range of k_{La} values there is a good agreement between the regression model and the simulation. For the low stirrer speeds and gassing rates however the simulated values are substantially lower than the one obtained by the regression model. Due to the Flow number and Froude number which are out of bounds of the prediction, a different flow regime inside the reactor leads to differing values. Also for the simulation for constant stirrer speed N the Froude and Flow number is out of bounds, the simulation shows higher values than the regression model.

6.3 Holdup

The holdup values from the simulations are compared to the regression model of the measured data in the same manner as for the k_{1a} value. The resulting values are shown in figure 6.6.

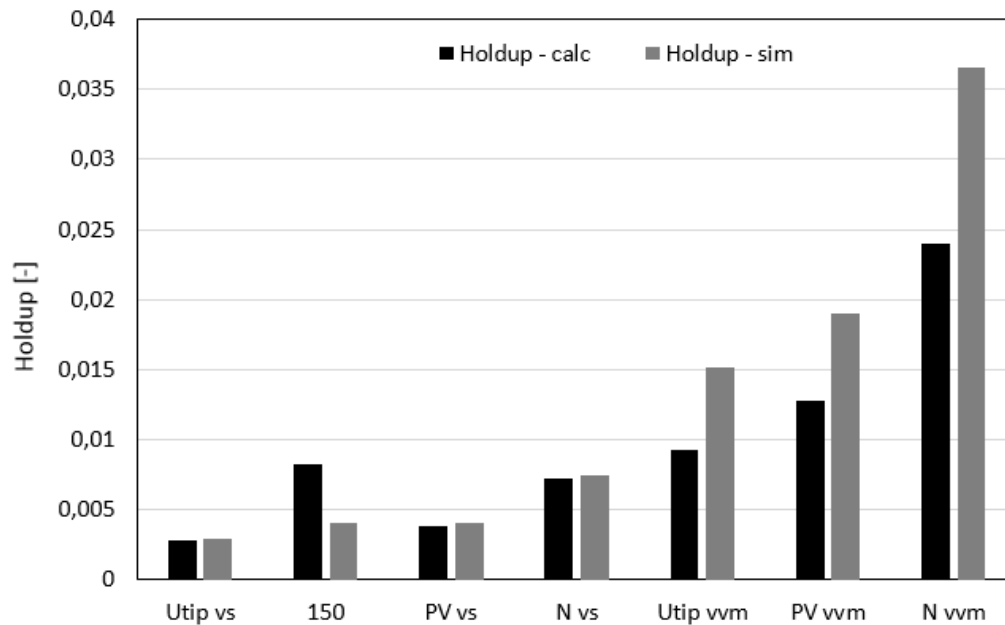


Figure 6.6: Comparison between Holdup of simulation and model prediction

Not all of the scaled up Froude numbers and Flow numbers lie within the range of the regression model described in chapter 2. For all scaled up simulations with a constant superficial velocity U_s the hold up corrections are in good agreement with the model. Especially for constant N and vvm simulation the holdup is too high. Again, here the Froude and Flow numbers are not within the regression bounds.

6.4 Shear Rate

The maximum shear rate, as well as the average shear rate is compared to the literature value from the correlations described in chapter 2.

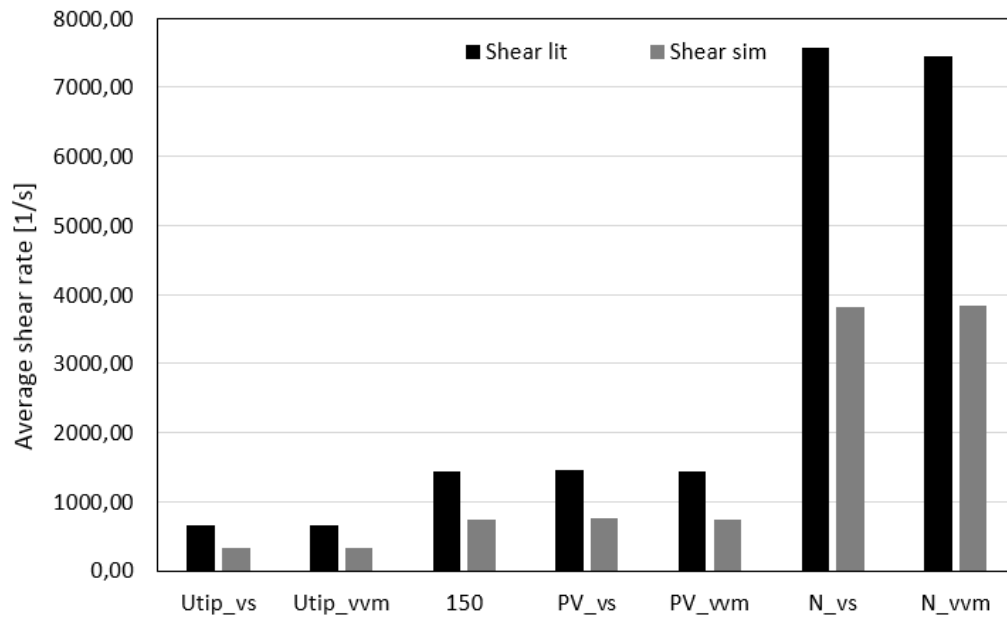


Figure 6.7: Comparison between average shear rate predicted and simulated

The average shear rate is shown to yield values half as large as the predicted values. In previous study [4] this issue is already discussed. The shear rate is not calculated at the boundary nodes, therefore these values are missing in the calculation of the average shear rate. The factor by which these values differ is different for the stirrer setup, a large number of boundary nodes results in a larger deviation in average shear rate. The deviation is constant here because the geometry stays the same in all simulations.

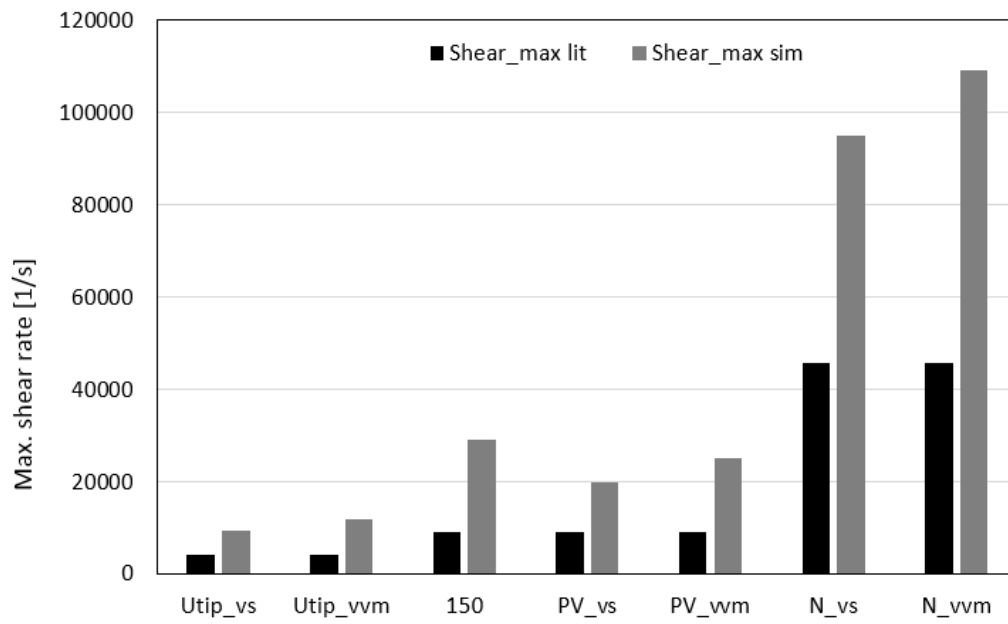


Figure 6.8: Comparison between maximum shear rate predicted and simulated

The maximum shear rate shows larger values as predicted. Previous simulations [4] showed that for finer grids, the values correlate better.

6.5 Summary

In this chapter the extended simulation code with the improved lattice unit calculation, the limitation for too high number of particles in a parcel, the newly implemented backward coupling for the species transport as well as the implemented simulation routine for multiple reactors in series is tested and applied on a standard 150 l gassed stirred tank reactor with triple Rushton turbines.

A geometrically similar reactor with a Scale-Up factor of 5 is tested with different operating conditions ranging from constant volumetric power input, constant stirrer speed, constant blade tip velocity, constant superficial gas velocity and constant volumetric gassing rate.

From the simulations, the $k_L a$ -values and the holdup is compared to a regression model based on the dimensionless Froude number and Flow number. Within the specified range of measurements, the results are in very good agreement. The mixing times for different homogeneities, the power input and the shear rates are compared with correlations from different authors and yield reasonable results.

Chapter 7

Small scale Simulations

The 20 l reactor is simulated with the following operating conditions:

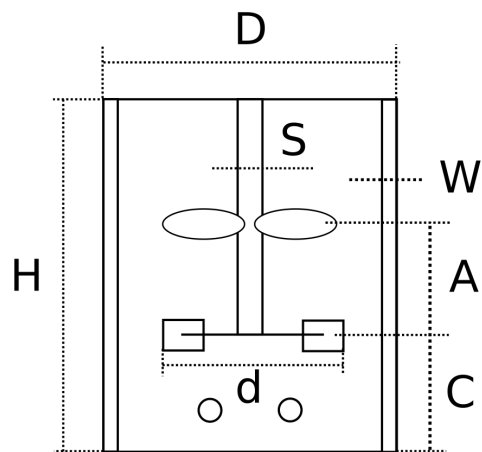


Table 7.1: Small scale operating conditions

Reactor	20 l	20 l	20 l
Stirrer speed [1/min]	20	20	20
Gas Flow Rate [l/min]	0	1	2

7.1 Mixing times

The mixing times have already been discussed in chapter 4.3 for this reactor setup.

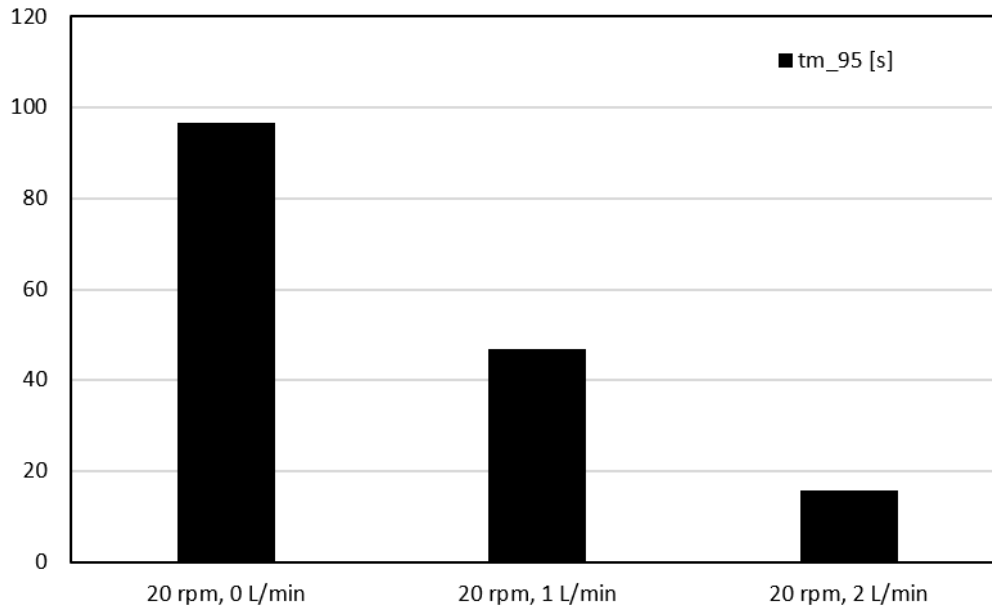


Figure 7.1: Mixing times in the 20 l reactor - new gas phase coupling

The values are decreasing with increased gassing rate as expected. The correlations described in chapter 2 can not be applied here because of the different stirrer setup with the newly implemented elephant ear impeller.

7.2 k_1a -value

The simulated k_1a values are compared with the dimensionless correlations given in chapter 2.

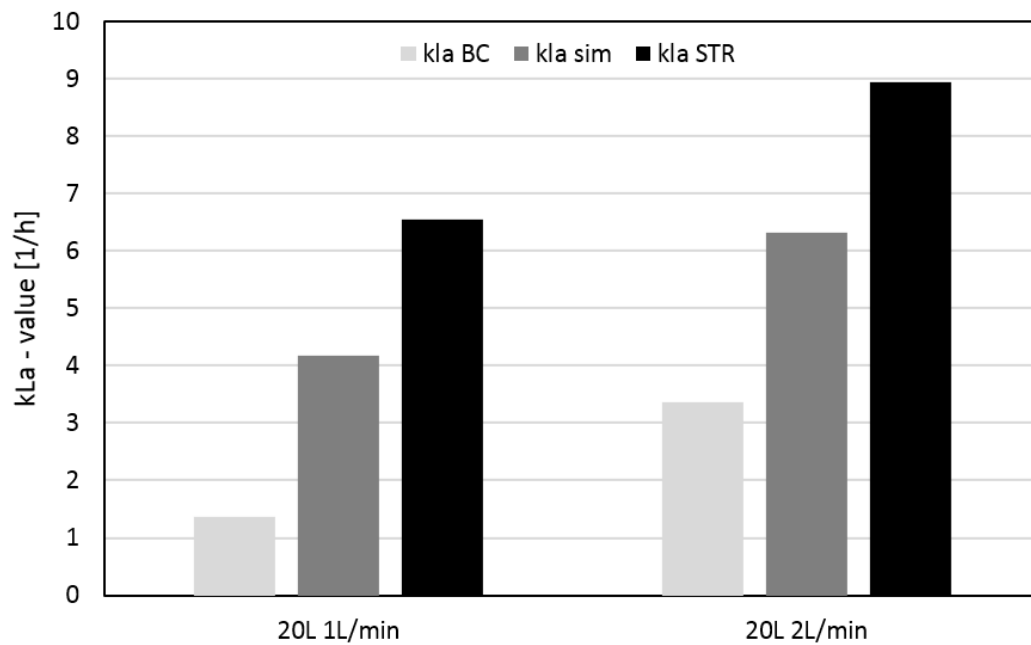


Figure 7.2: kLa values in the 20 l reactor

In figure 7.2 the obtained values are shown. The lower values are obtained from the correlation for a bubble column without stirrers attached. The upper bound is from the dimensionless equation for a standard gassed stirred tank. It can be seen that the simulated k_1a values are very well in between these bounds. A full dispersion like in a standard gassed stirred tank is not reached but the values are higher than for the bubble column, as expected.

7.3 Shear Rates

The obtained average shear rates are compared with the correlations given in chapter 2.

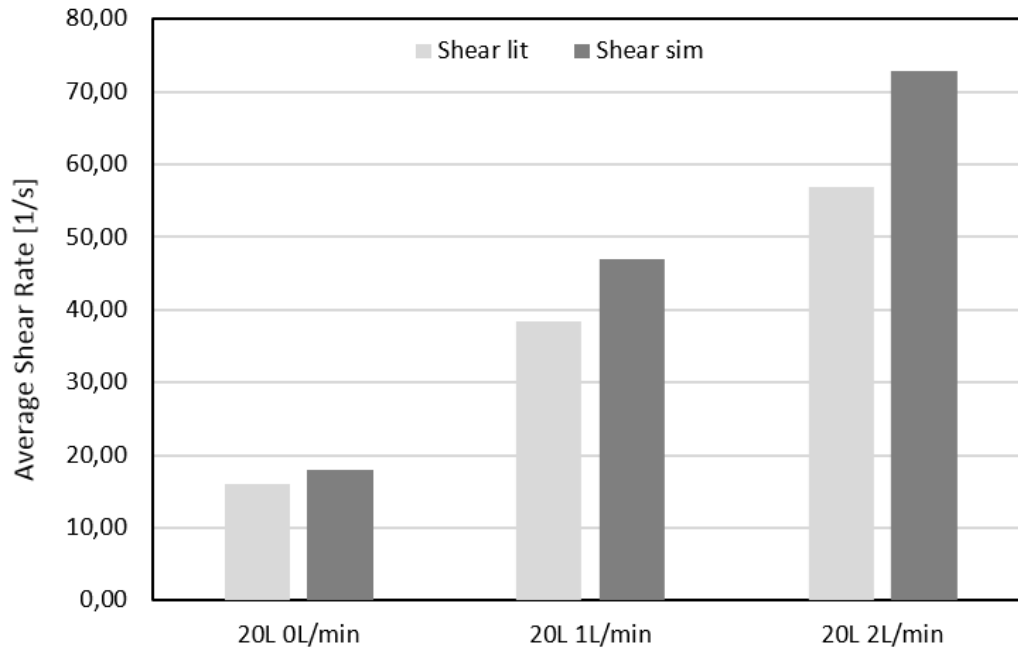


Figure 7.3: Average shear rate in the 20 l reactor

The average shear rate shows good agreement with the predictions from Perez et. al. [12]. However for larger gassing rates an overestimation can be seen.

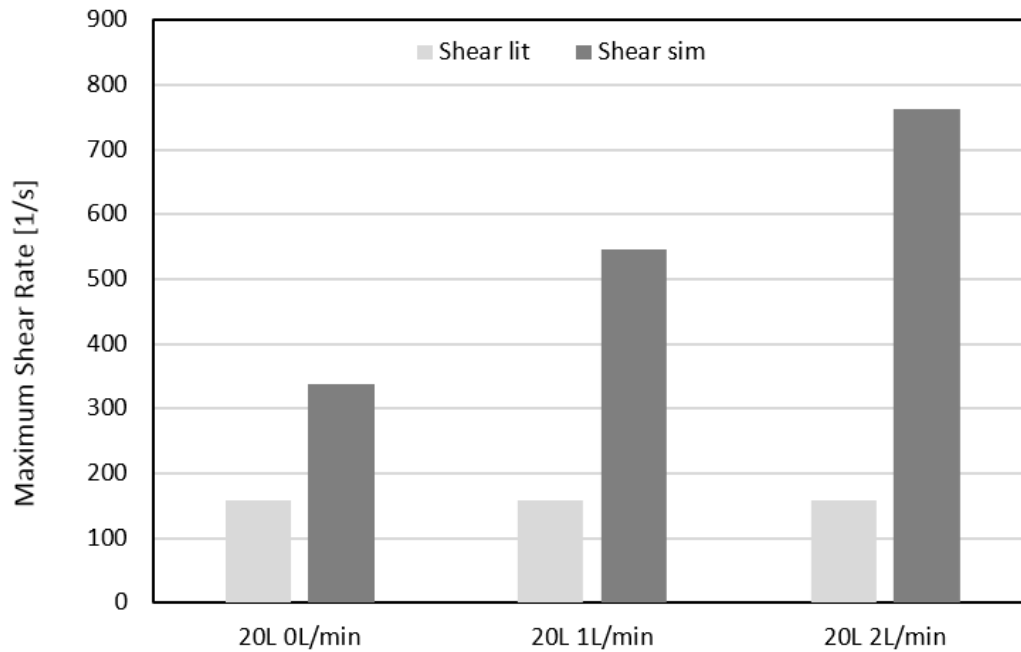


Figure 7.4: Maximum shear rate in the 20 l reactor

The maximum shear rate is expected to rise with higher gassing rates. However the correlation from Wichterle et. al. [21] does not account for any gassing rate or gassed power input, therefore the value is constant. For the ungassed small scale reactor the overprediction factor of 2 can be seen, just like in the Scale-Up simulations. With increased gassing rate this deviation becomes larger as expected.

7.4 Non-Newtonian fluid

Table 7.2: 20L reactor with non Newtonian fluid

Reactor	20 l
Stirrer speed [1/min]	300
Gas Flow Rate [l/min]	1
Power Law Coefficient K [$kg s^{n-2}/m$]	0.0367
Power Law index n [-]	0.65
Density ρ [kg/m^3]	1000
Surface Tension σ [N/m]	0.069

The average shear rate and the maximum shear rate are again compared with the same correlations as for the previous Scale-Up and small scale simulations. For the $k_l a$ -value the equation from chapter 2 for non-Newtonian fluids is used. This correlation is valid for stirred tanks, which is a reasonable assumption for this simulation because of the higher stirrer speed than with the previous small scale simulations. The following values are obtained:

Table 7.3: Results of the non-Newtonian small scale simulation

	Correlation	Simulation
Average Shear Rate [1/s]	494.69	554.235
Maximum Shear Rate [1/s]	7614.712	10920
$k_l a$ -value [1/h]	20.175	23.441

The results are generally in good agreement. Average shear rate and $k_l a$ -value show a slight overprediction, whereas the maximum shear rate deviates larger. This is already seen in the previous simulations in this thesis.

7.5 Summary

The improved simulation code is tested on a small scale reactor with operating conditions ranging from very low stirrer speed to higher stirring speeds with Non-Newtonian fluids. In these simulations the newly implemented elephant-ear-impeller is used. The obtained k_La -values and shear rates are compared to correlations from different authors which described equations for bubble columns as well as gassed stirred tank reactors.

Since the stirrer speed is set to a low stirrer speed compared to standard stirred tank setup, the obtained k_La values are lower than for usual stirred tanks, because of the insufficient gas dispersion. However by comparison with k_La values for bubble columns, we can see that the simulated mass transfer values lie very well between these two operating regimes.

For the Non-Newtonian case a power law fluid was tested with a higher stirrer speed, and the correlation from Costa et. al. [3] is in good agreement with the simulated k_La value.

Chapter 8

Summary

In the present thesis an existing simulation code for stirred tank reactors is extended and applied on different reactor sizes with varying operating conditions. The first goal was to implement internal tank geometries which includes a new stirrer type, the so-called elephant ear impeller, next to the already implemented Rushton turbines. Additionally, detailed geometries like sensors that reach into the fluid region can now be specified. A more complex implementation of tank geometries is made for the heat exchangers. Since the grid resolution of the fluid simulation is too coarse to resolve single heat exchanger tubes, a macroscopic porous media model [15] is applied.

For the Scale-Up simulations a scaling factor of 5 is applied on a pilot plant 150 l reactor. For the comparison of the simulations the mixing time, the volumetric mass transfer coefficient, the gas hold-up, the power input as well as the shear rate are compared. Correlations for the mixing time [5], the power input [10] and the shear rate [21] [12] are found in published literature. An empirical correlation for k_1a -value and holdup is found by regression from measurements.

Before applying the simulation code numerous improvements are made: The boundary condition for the species transport model is changed to a free-slip condition and the boundary nodes are set with an artificial diffusion to reduce de-mixing effects at the boundary. A new consideration of the gas phase coupling onto to the fluid phase is able to predict a consistent mixing behaviour for increased gassing rates. The oxygen saturation curves yield too high mass transfer coefficients. By reducing the time step in which mass transfer is calculated, the k_1a -values correlate very well with experimental data. In the new code the bubble rising velocity is considered in the simulation setup for the estimation of the highest velocity inside the reactor. The parcel approach for the gas phase is now ensured to be initialised correctly by comparing the parcel volume with the cell volume. In addition to these improvements an automated serial simulation routine is implemented.

The results are in very good agreement for the k_1a -values, power numbers and mixing times and in good agreement with holdup values. The average shear rate is underpredicted, whereas the maximum shear rate is overpredicted. A small reactor is tested with the new stirrer geometry and the k_1a -value shows good agreement with dimensionless correlations [12] [1] even for non-Newtonian fluids [3].

Bibliography

- [1] Kiyomi Akita and Fumitake Yoshida. "Gas Holdup and Volumetric Mass Transfer Coefficient in Bubble Columns. Effects of Liquid Properties". In: *Industrial & Engineering Chemistry Process Design and Development* 12.1 (1973), pp. 76–80.
- [2] P. L. Bhatnagar, E.P. Gross, and M. Krook. "A Model for Collision Processes in Gases. I. Small Amplitude Processes in Charged and Neutral One-Component Systems". In: *Physical Review* 94 (1954), pp. 511–525.
- [3] E Costa et al. "Transferencia de materia en tanques agitados: burbujeo de gases en líquidos newtonianos y no newtonianos. I. Turbinas de 6 paletas y difusor plano". In: *An Quim* 78 (1982), pp. 387–92.
- [4] Philipp Eibl. "Bachelor Thesis: Simulation of shear rates and power consumption of stirred tanks". Institute for Process and Particle Engineering, Graz University of Technology, 2016.
- [5] J.B. Fasano, Andre Bakker, and W.R. Penney. "Advanced impeller geometry boosts liquid agitation". In: *Chemical Engineering (New York); (United States)* 101:8 (Aug. 1994).
- [6] J. J. J. Gillissen and H. E. A. Van den Akker. "Direct numerical simulation of the turbulent flow in a baffled tank driven by a Rushton turbine". In: *AIChE Journal* 58.12 (2012), pp. 3878–3890. ISSN: 1547-5905.
- [7] Y. Kawase and M. Moo-Young. "Mixing time in bioreactors". In: *Journal of Chemical Technology and Biotechnology* 44.1 (1989), pp. 63–75. ISSN: 1097-4660.
- [8] Matthias Kraume. *Transportvorgänge in der Verfahrenstechnik*. Springer, 2003. ISBN: 3-540-40105-9.
- [9] Alessandro Paglianti. "Simple Model to Evaluate Loading/Flooding Transition in Aerated Vessels Stirred by Rushton Disc Turbines". In: *The Canadian Journal of Chemical Engineering* 80.4 (2002), pp. 1–5. ISSN: 1939-019X.
- [10] Edward L. Paul, Victor A. Atiemo-Obeng, and Suzanne M. Kresta. *Handbook of Industrial Mixing*. Wiley-Interscience, 2003.
- [11] Jerome F. Perez and Orville C. Sandall. "Gas absorption by non-Newtonian fluids in agitated vessels". In: *AIChE Journal* 20.4 (1974), pp. 770–775. ISSN: 1547-5905.
- [12] Sanchez J. A. Perez et al. "Shear rate in stirred tank and bubble column bioreactors". In: *Chemical Engineering Journal* 124 (2006), pp. 1–5.

- [13] em. Professor Dr.-Ing. Dr. techn.E.h. Jürgen Zierep. *Grundzüge der Strömungslehre*. 9th ed. Springer-Vieweg, 2013. ISBN: 978-3-658-01605-0.
- [14] R. Sander. "Compilation of Henry's law constants (version 4.0) for water as solvent". In: *Atmospheric Chemistry and Physics* 15.8 (2015), pp. 4399–4981.
- [15] Michael C. Sukop and Daniel T. Thorne. *Lattice Boltzmann Modeling - An Introduction for Geoscientists and Engineers*. Springer, 2006. ISBN: 978-3-540-27982-2.
- [16] Radompon Sungkorn. "Euler-Lagrange Modeling of dispersed Gas-Liquid Reactors". PhD thesis. Institute for Process and Particle Engineering, Graz University of Technology, 2011.
- [17] Mario Talaia. "Terminal Velocity of a Bubble Rise in a Liquid". In: *World Acad. Sci. Eng. Technol.* 28 (2007), pp. 264–268.
- [18] Nils Thürey. "Physically based Animation of Free Surface Flows with the Lattice Boltzmann Method". PhD thesis. Technische Fakultät der Universität Erlangen-Nürnberg, 2007.
- [19] Erlend Magnus Viggen. "The Lattice Boltzmann Method: Fundamentals and acoustics". PhD thesis. Department of Physics, Norwegian University of Science and Technology, 2014.
- [20] Erlend Magnus Viggen. "The Lattice Boltzmann Method with Applications in Acoustics". MA thesis. Department of Physics, Norwegian University of Science and Technology, 2009.
- [21] Kamil Wichterle et al. "Shear rates on Turbine Impeller Blades". In: *Chemical Engineering Communications* 26:1-3 (1984), pp. 25–32.
- [22] Huidan Yu, Sharath S. Girimaji, and Li-Shi Luo. "DNS and LES of decaying isotropic turbulence with and without frame rotation using lattice Boltzmann method". In: *Computational Physics* 209 (2005), pp. 599–616.

List of Figures

1.1	D3Q19-Lattice	2
1.2	Parcel approach for the gas phase	6
1.3	D3Q27-Model	10
1.4	Geometry of the 25 liter vessel	12
1.5	Geometry of the 150 liter vessel	12
1.6	Geometry of the 19 m^3 vessel	12
2.1	Example of normalized conductivity probe responses[10, p. 173]	14
2.2	Regression model of the measured mass transfer data	20
2.3	Regression model of the measured holdup data	22
2.4	Newton number over Reynolds number[10, p. 361]	23
3.1	Reactor with bottom Rushton turbine and top elephant ear impeller	25
3.2	Grid adaption for the heat exchanger model	27
3.3	Heat exchanger model - top view of the flow field	28
3.4	Heat exchanger model - side view of the flow field	28
3.5	Sensor parameters - top view	30
3.6	Sensor parameters - side view	30
4.1	Bounce-back and free-slip condition	32
4.2	Mixing times in the 20 Liter reactor	33
4.3	Gas phase coupling with added coupling force	34
4.4	Gas phase coupling with subtracted coupling force	34
4.5	Mixing times in the 20 Liter reactor - new gas phase coupling	35
4.6	Simulated oxygen concentration over time	36
4.7	Mass transfer from gas phase to fluid phase	37
5.1	Bubble displacement for too high bubble volumes in a cell	40
5.2	Start of a simulation series	41
5.3	Compiling and running a simulation series	42
5.4	Restart routine for a simulation series	43
6.1	Mixing times for the 150 l Reactor	47
6.2	Mixing times for the 19 m^3 Reactor with constant U_{tip}	48
6.3	Mixing times for the 19 m^3 Reactor with constant P/V	49
6.4	Mixing times for the 19 m^3 Reactor with constant N	50

6.5	Comparison between $k_L a$ of simulation and model prediction	51
6.6	Comparison between Holdup of simulation and model prediction	52
6.7	Comparison between average shear rate predicted and simulated	53
6.8	Comparison between maximum shear rate predicted and simulated	54
7.1	Mixing times in the 20 l reactor - new gas phase coupling	57
7.2	$k_L a$ values in the 20 l reactor	58
7.3	Average shear rate in the 20 l reactor	59
7.4	Maximum shear rate in the 20 l reactor	60

List of Tables

3.1	Elephant-ear impeller parameters	26
3.2	Sensor parameters	29
4.1	Species initialisation parameters	31
6.1	Scale up operating conditions	44
6.2	Froude number and Flow number for the Scale-Up simulations	45
6.3	Results of power input for the Scale-Up simulations	46
7.1	Small scale operating conditions	56
7.2	20L reactor with non Newtonian fluid	61
7.3	Results of the non-Newtonian small scale simulation	61

Appendix A

Appendix

A.1 Nomenclature

f_i	[-]	Probability density function
x_i	[-]	Spatial coordinate in lattice units
c_i	[-]	Velocity in lattice units
Ω_i	[-]	Collisional operator
c_s	[-]	Speed of sound in lattice units
τ	[-]	Relaxation time in lattice units
ρ	$[kg/m^3]$	Density
δx	$[m]$	LBM Conversion factor for length
δt	$[s]$	LBM Conversion factor for time
δm	$[kg]$	LBM Conversion factor for mass
D, D_L	$[m^2/s]$	Diffusion coefficient
$S, \dot{\gamma}$	$[1/s]$	Shear rate magnitude
$S_{\alpha\beta}$	$[1/s]$	Shear rate tensor
ν	$[m^2/s]$	Kinematic viscosity
ν_{eff}	$[m^2/s]$	Effective viscosity
ν_{app}	$[m^2/s]$	Apparent viscosity
ν_t	$[m^2/s]$	Turbulent viscosity
$\Pi_{\alpha\beta}$	[-]	Non-equilibrium stress tensor in lattice units
C	[-]	Smagorinsky constant
$\mathbf{F}_{p,i \rightarrow l,j}$	$[N]$	Backward coupling force
K	$[kgs^{n-2}/m]$	Power law coefficient
n	[-]	Power law index
ϵ	$[W/m^3]$	Energy dissipation rate
Pe	[-]	Peclet number
Re	[-]	Reynolds number
Sc	[-]	Schmidt number
Fr	[-]	Froude number
Fl	[-]	Flow number
N_p	[-]	Power number

k_l	[m/s]	Mass transfer coefficient
$k_l a$	[1/s]	Volumetric mass transfer coefficient
t_c	[s]	Contact time
MW	[kg/kmol]	Molecular weight
$H_{x,p}$	[Pa ⁻¹]	Henry constant
A	[m ³]	Surface area
c^*	[kmol/m ³]	Saturation concentration
ϕ	[-]	Holdup
V_G	[m ³]	Gas volume
V_L	[m ³]	Liquid volume
V_R	[m ³]	Reactor volume
P	[W]	Power
t_m	[s]	Mixing time
k_m	[1/s]	Mixing rate constant [5]
T	[m]	Stirrer diameter
D	[m]	Tank diameter
σ	[N/m]	Surface Tension
μ_G	[kg/(ms)]	Dynamic gas viscosity
μ_a	[kg/(ms)]	Dynamic apparent liquid viscosity
U_s	[m/s]	Superficial gas velocity
Q	[m ³ /h]	Gas flow rate
g	[m/s ²]	Gravitational acceleration
n_S	[-]	Solid fraction
vvm	[min ⁻¹]	Volumetric gas flow rate
<i>calc</i>		Calculated from regression model
<i>sim</i>		Simulated value
<i>lit</i>		Calculated value from published correlation
<i>BC</i>		Bubble column
<i>STR</i>		Stirred tank reactor

A.2 $k_{l}a$ measurements on the 150 L reactor

N [min ⁻¹]	Q [m ³ /h]	$k_{l}a$ [1/s]
195	0.74	0.0051
190	1.8	0.007013926
250	1.8	0.0112
190	16	0.0179
450	1.7	0.019096
200	18	0.019711
430	1.6	0.022177
490	5	0.0288

A.3 Hold-Up measurements on the 150 L reactor

N [min ⁻¹]	Q [m ³ /h]	ϕ [%]
197	0.75	1.281
195	0.74	1.3976
200	0.7	1.700
250	1.8	1.9963
200	1.9	1.9963
250	1.9	2.4952
270	1.8	2.4954
280	1.833	2.5296
450	1.8	3.4923
450	1.7	3.4936
440	1.7	3.4936
450	1.7	3.5
500	1.9	3.9912
500	2.5	4.2990
490	4.6	5.9888
490	5	7.4179
350	8	8.9803
355	8	9.0591